April 1991 • SERI/TP-214-4292

PROPERTY OF
U. S. GOVERNMENT

Research on Stable, High-Efficiency Amorphous Silicon Multijunction Modules

Semiannual Subcontract Report
1 August 1989 - 31 January 1991

SOLAR ENERGY RESEARCH INSTITUTE
TECHNICAL LIBRARY

MAY 23 1991

GOLDEN, COLORADO 80401

P.K. Bhat, S. Brown, R. Hollingsworth,
D.S. Shen, J. del Cueto, E. Iwanicko,
C. Marshall, C. DeHart, D. Mentor,
A. Benson, C. Matovich, J. Sandwisch
Glasstech Solar, Inc.
Golden, Colorado

Solar Energy Research Institute
A division of Midwest Research Institute
Operated for the U.S. Department of Energy
under contract No. DE-AC02-83CH10093

SERI/TP-214-4292 c.3

SERI/TP-214-4292 • UC Category: 271 • DE91002159

SERI/TP--214-4292

DE91 002159

Research on Stable, High-Efficiency Amorphous Silicon Multijunction Modules

Semiannual Subcontract Report 1 August 1989 - 31 January 1991

P.K. Bhat, S. Brown, R. Hollingsworth, D.S. Shen, J. del Cueto, E. Iwanicko, C. Marshall, C. DeHart, D. Mentor, A. Benson, C. Matovich, J. Sandwisch
Glasstech Solar, Inc.
Golden, Colorado

SERI technical monitor: W. Luft

Solar Energy Research Institute
1617 Cole Boulevard
Golden, Colorado 80401-3393
A Division of Midwest Research Institute
Operated for the U.S. Department of Energy
under Contract No. DE-AC02-83CH10093

Prepared under Subcontract No. ZM-0-19033-3

April 1991

MASTER

This publication was reproduced from the best available camera-ready copy submitted by the subcontractor and received no editorial review at SERI.

NOTICE

This report was prepared as an account of work sponsored by an agency of the United States government. Neither the United States government nor any agency thereof, nor any of their employees, makes any warranty, express or implied, or assumes any legal liability or responsibility for the accuracy, completeness, or usefulness of any information, apparatus, product, or process disclosed, or represents that its use would not infringe privately owned rights. Reference herein to any specific commercial product, process, or service by trade name, trademark, manufacturer, or otherwise does not necessarily constitute or imply its endorsement, recommendation, or favoring by the United States government or any agency thereof. The views and opinions of authors expressed herein do not necessarily state or reflect those of the United States government or any agency thereof.

Printed in the United States of America
Available from:
National Technical Information Service
U.S. Department of Commerce
5285 Port Royal Road
Springfield, VA 22161

Price: Microfiche A01
Printed Copy A04

Codes are used for pricing all publications. The code is determined by the number of pages in the publication. Information pertaining to the pricing codes can be found in the current issue of the following publications which are generally available in most libraries: *Energy Research Abstracts (ERA)*; *Government Reports Announcements* and Index (*GRA* and I); *Scientific and Technical Abstract Reports (STAR)*; and publication NTIS-PR-360 available from NTIS at the above address.

Table of Contents

		Page
1.0	SUMMARY	7
2.0	TASK I: SEMICONDUCTOR MATERIALS AND DEVICE RESEARCH	8
	2.1 I-Layer Band Gap Adjusting	8
	2.1.1 Effect of Deposition Temperature	8
	2.1.2 Hydrogen Dilution	11
	2.1.3 Effect of Electrode Distance	13
	2.2 Device Fabrication	13
	2.2.1 Low Temperature Device	13
	2.2.2 High Temperature Device	16
	2.2.3 NIP Devices With High Temperature I-Layer	20
	2.2.4 Devices With I-Layers Deposited With Hydrogen Dilution	20
	2.3 Stability	22
	2.3.1 Long Term Stability of Tandem Cells	22
	2.3.2 Stability vs. Deposition Conditions	25
	2.3.3 Stability vs. Deposition Temperature	34
	2.3.4 Stability of the High Bandgap Cell	39
	2.3.5 Stability of the Cells With I-Layers Deposited With Hydrogen Dilution	44
	2.4 Thin Microcrystalline P-Layers	46
	2.5 Device Modeling	48
3.0	TASK II: NON-SEMICONDUCTOR RESEARCH	55
	3.1 ITO/Ag Back Reflector	55
	3.2 Stability of Top Contacts	58
	3.3 Transparent Conductive Oxide	58
	3.3.1 Equipment and Process Description	58
	3.3.2 Results	61
4.0	TASK III: MODULE RESEARCH	65
5.0	CONCLUSION	67

Figure Captions

Fig. 1	The photoconductivity and dark conductivity vs. the deposition temperature
Fig. 2	The optical properties vs. the deposition temperature
Fig. 3	The conductivities vs. the H_2/SiH_4 ratio
Fig. 4	The Tauc's gap vs. the hydrogen dilution
Fig. 5	The photovoltaic parameters vs. the thickness of the intrinsic layer
Fig. 6	The biased quantum efficiency
Fig. 7	The quantum efficiency of a tandem device
Fig. 8	The photovoltaic parameters vs. the hydrogen dilution
Fig. 9	The normalized efficiency vs. the light soaking time
Fig. 10	The efficiency vs. the light soaking time
Fig. 11	The normalized open circuit voltage vs. the light soaking time
Fig. 12	The normalized short circuit current density vs. the light soaking time
Fig. 13	The normalized fill factor vs. the light soaking time
Fig. 14	The efficiency vs. the r.f. power density
Fig. 15	The efficiency vs. the deposition temperature
Fig. 16	V_{oc} versus light soaking time. The i-layers of device were deposited at different temperatures, as marked on the figure.
Fig. 17	J_{sc} versus light soak time.
Fig. 18	The fill factor versus the light soaking time. The symbols are the same as before.
Fig. 19	The efficiency versus the light soaking time. Note that the device has 330° i-layer is stable, but absolute efficiency is low.
Fig. 20	The photoconductivity of i-layers versus the light soaking time. Deposition temperatures are marked on the figure. Note that the photoconductivity of high temperature i-layers also drops.

Fig. 21 γ(where $\sigma_{ph} \alpha G^{\gamma}$) versus light soaking time. Note that γ's do not decrease.

Fig. 22 Normalized fill factor (after 600 hours light soaking) versus i-layer deposition temperature. Note that in certain temperature ranges, the normalized FF is constant.

Fig. 23 The efficiency vs. light soaking time for devices with different i-layer thicknesses.

Fig. 24 The normalized fill factor vs. light soaking time for devices with different i-layer thicknesses.

Fig. 25. The initial and degraded efficiency vs. the intrinsic layer thickness.

Fig. 26 The initial and degraded open circuit voltage vs. the intrinsic layer thickness.

Fig. 27 The absolute and normalized efficiency vs. the light soaking time for devices having intrinsic layers made with various hydrogen dilutions.

Fig. 28 The conductivity of microcrystalline p layers vs. thickness.

Fig. 29 The modeled photon absorption in each layer of a tandem.

Fig. 30 The modeled short circuit current vs. the band gap of the bottom cell.

Fig. 31 The modeled QE and IV of current tandem cells.

Fig. 32 The modeled QE and IV of future tandem cells.

Fig. 33 The modeled IV of the final goal tandem cell.

Fig. 34 The short circuit current for devices with ITO/Ag and Ag top contacts.

Fig. 35 The efficiency and percent degradation after 300 hours for devices with ITO/Ag and Ag top contacts.

Fig. 36 The tin oxide injector schematic.

Fig. 37 The tin oxide sheet resistance, transmission, haze and resistivity vs. the injector height.

Fig. 38 The tin oxide sheet resistance, resistivity, thickness and haze vs. the methanol to water ratio.

Fig. 39 IV curve of a subcell of a large area ($4800cm^2$) tandem panel.

List of Tables

Table 1 Photovoltaic parameters of n-i-p cells

Table 2 Light soaking effect on the tandem cells

Table 3 Intrinsic layer deposition conditions

Table 4 Initial performance of devices with Ag and ITO/Ag back contacts. The column labeled "ITO/Ag-Ag" is obtained by subtracting the performance within each run.

Table 5 # Parameters of large area panels measured at SERI

1.0 SUMMARY

The purpose of this research during Phase I, (12 months), has been to develop all-amorphous-silicon-alloy based, multijunction modules having an aperture area of at least 900 cm^2 with a stable, reproducible conversion efficiency of at least 6.5% after 600 hours light exposure (AM1.5) at 50°C.

The effort was focused on 1) producing opto-electronic grade a-Si:H material for band gaps of about 1.7 eV and 1.9 eV, by changing the hydrogen content in the film which is bonded to silicon, 2) studying and obtaining data on light stability of single-junction p-i-n solar cells with gaps about 1.7 eV and 1.9 eV, and 3) analyzing losses in a silicon-silicon multijunction cell.

Progress was made on use of ITO/Ag as a back contact. The current density can be increased by about 1-2 mA/cm^2. Thin films of SnO_2 deposited by the APCVD method over areas of 40 x 120 cm^2 were successfully produced with good opto-electronic properties. Amorphous silicon-silicon multijunction modules of 40 x 120 cm^2 area, were fabricated during this period. Some of these modules were measured at SERI. Results on these modules suggest that much improvement in efficiency can be expected by simply incorporating the results obtained on small area cells.

Progress toward the goal has been good with the demonstration of 5.4% initial efficiency in a silicon-silicon multijunction module having an aperture area of 4620 cm^2 and incorporating devices with dual-junction i-layer thicknesses of ~3500Å. Moreover, a single-junction silicon module having an aperture area of 4620 cm^2 and a thickness of ~3500Å with initial efficiency of 6.5% was demonstrated.

Although there were no stability experiments performed on these modules, a comparison with small area stability results indicates the efficiency of the Si-Si tandem modules should approach 4.4% after 600 hours of light soaking.

2.0 TASK I: SEMICONDUCTOR MATERIALS AND DEVICE RESEARCH

2.1 i-layer Band Gap adjusting

Ideally, a high-band-gap i-layer is preferred for the top cell (to gain high V_{oc}) and a low-band-gap i-layer is preferred for the bottom cell (to gain in red current). Without alloying (e.g., with carbon or germanium), the band gap is adjusted through changing hydrogen concentration in the material. Two problems have to be addressed: initial electronic properties and stability. In general, the initial electronic properties will degrade when the hydrogen concentration deviates from the optimized value. Furthermore, for low-hydrogen material fabricated at high temperatures, the impurities from out-gassing of the deposition chamber are an extra concern. For high-hydrogen intrinsic Si:H material, light stability is a concern.

Three approaches were pursued, namely 1) changing the deposition temperature, 2) diluting of silane gas with hydrogen, and 3) changing the deposition chamber interelectrode distance in a parallel plate electrode configuration.

To control the impurity in the low-band-gap material deposited at high temperatures, we increased pumping speed and time to ensure a low baseline pressure (below 2×10^{-8} Torr). We used higher gas flow (80 sccm) and low r.f. power density (~20 mW/cm^3) to improve the electronic properties.

2.1.1 Effect of Deposition Temperature:

Figure 1 shows the photoconductivity (AM1.5 100 mW/cm^2 and under 600 nm filter light) and dark conductivity vs. the deposition temperature.

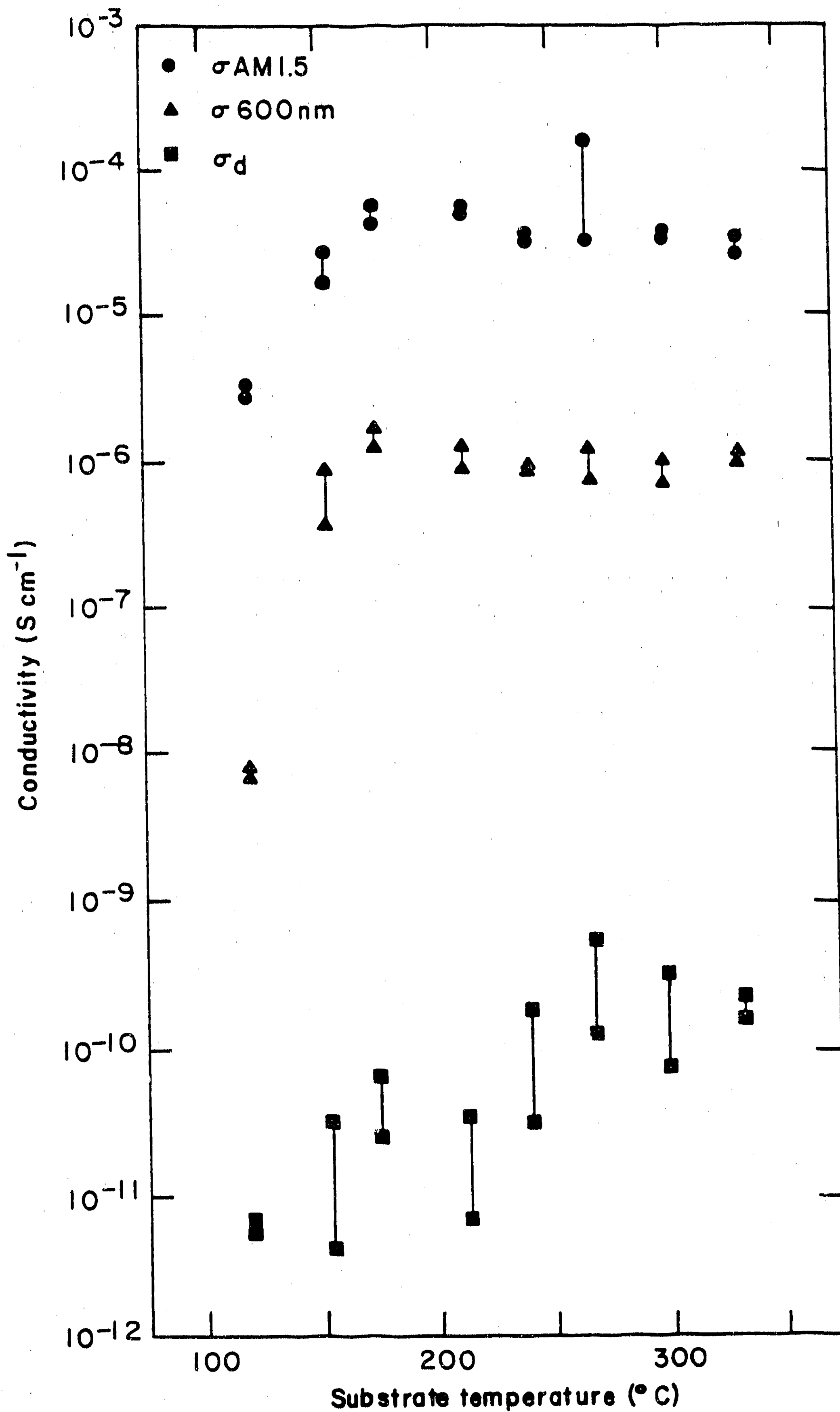

Figure 1. The photoconductivity and dark conductivity versus the deposition temperature

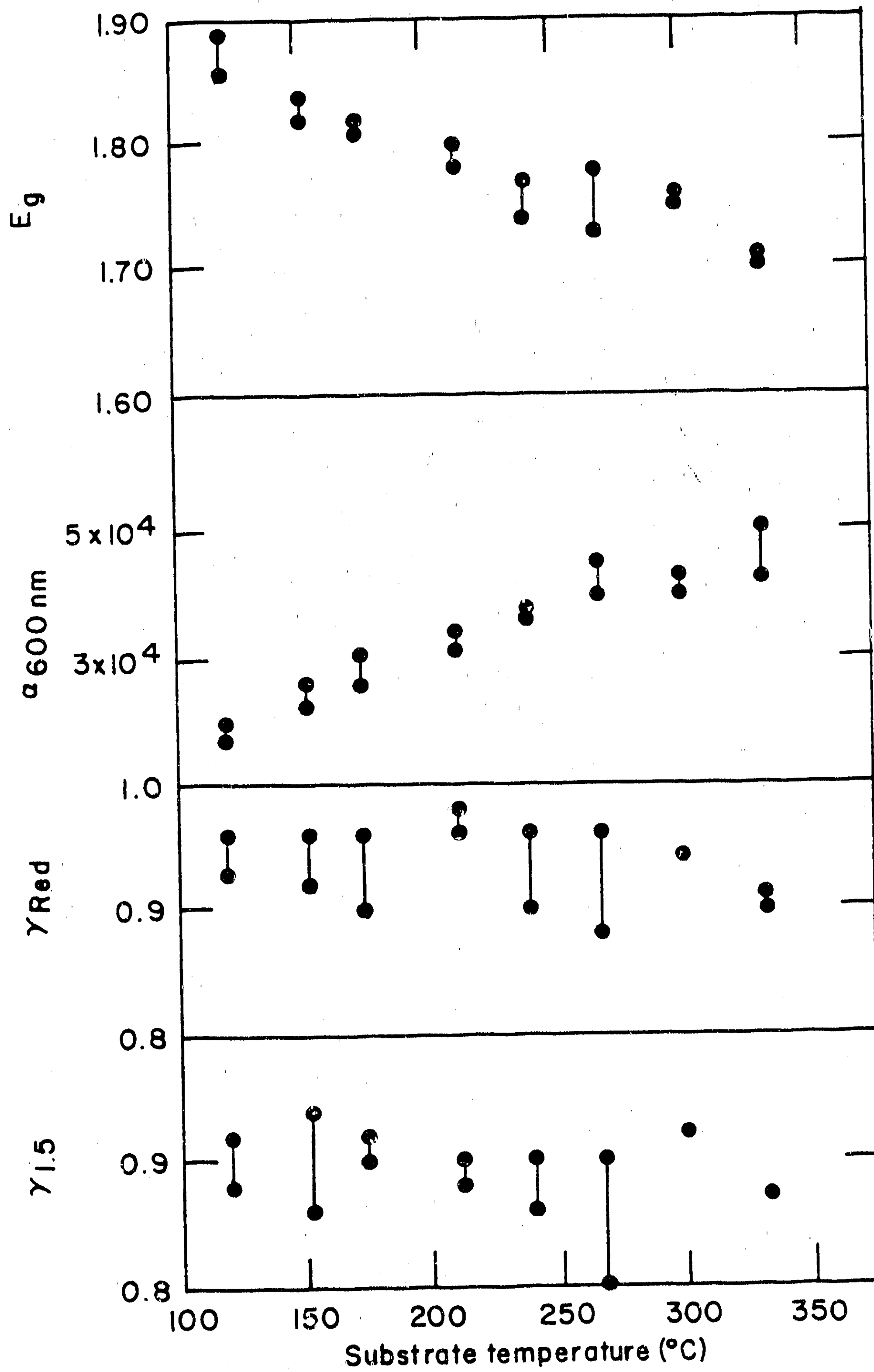

Figure 2. The optical properties versus the deposition temperature.

Figure 2 shows the optical gap Eg, the absorption coefficient at 600 nm wavelength, and the power index γ of photoconductivity for red light and AM1.5 light plotted against the deposition temperature.

These results suggest that the photoconductivity remains constant until the deposition temperature dropps below 150°C. The dark conductivity increased by about one order of magnitude when the band gap decreased from 1.83 eV to 1.70 eV. The photosensitivity is on the order of 10^5. The band gap decreased and the red absorption coefficient increased linearly as the deposition temperature increased. The activation energy of the dark conductivity was also measured to estimate the position of the Fermi level. For an i-layer with σ Tauc gap of 1.70 eV, the activation energy was 0.85 eV. This activation energy and good electronic propertie_ as shown in Figure 1 and Figure 2 suggest that the impurities level in the intrinsic layer was low. We believe that the electronic properties of these materials are good enough to be used in tandem cells.

2.1.2 Hydrogen Dilution

From previous work on the devices we know that it is difficult to fabricate good devices at high temperatures of deposition. Thus, we examined the use of heavy hydrogen dilution as an alternative. It is well known that very heavy hydrogen dilution can reduce the hydrogen content in films through an etching reaction with atomic hydrogen[1]. Microcrystalline films with 2-3% hydrogen content are produced in this manner. The approach we pursued here was to operate in the regime just short of microcrystalline formation where the hydrogen content in the film would be around 5-7%, and presumably the film would be amorphous with a low band gap. To enhance the hydrogen radical concentration, we used high frequency (110 MHz) plasma, since we have previously observed stronger atomic hydrogen emission from high frequency plasmas using optical emission spectroscopy[2].

Figure 3 shows the light and dark conductivities of the layers as a function of the H_2/SiH_4 ratio. The photoconductivity remains relatively

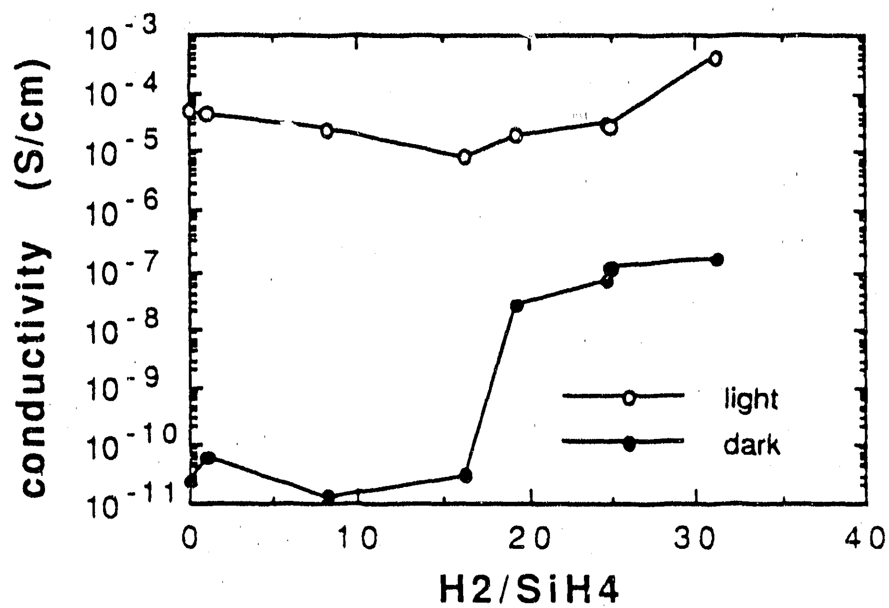

Figure 3. The conductivities vs. the H_2/SiH_4 ratio

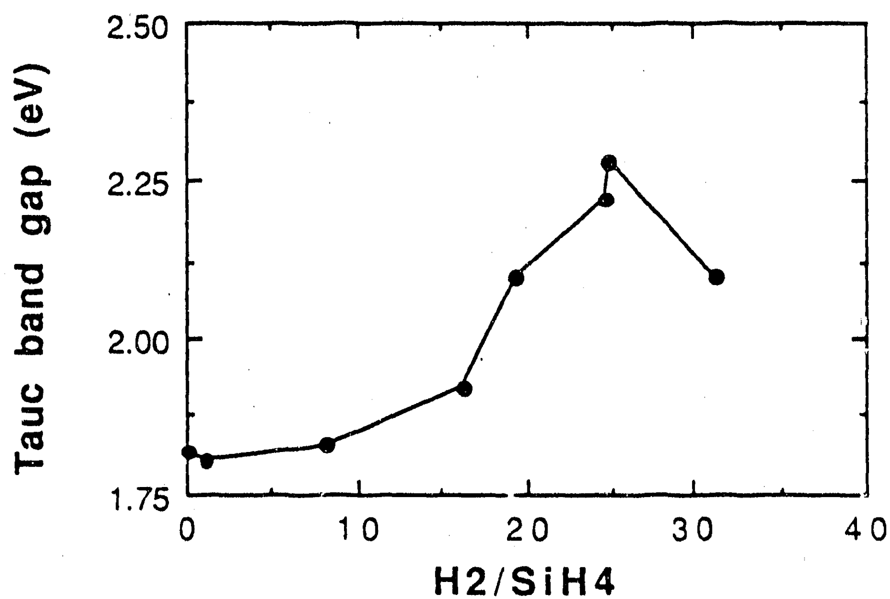

Figure 4. The Tauc's gap vs. the hydrogen dilution

constant but the increase in dark conductivity at H_2/SiH_4 of 20 suggests that microcrystalline films were being formed. Figure 4 shows the Tauc band gap of the films plotted against the hydrogen dilution ratio. Contrary to the expectation, there is a monotonic increase in band gap as hydrogen dilution increases. Raman scattering was done on three films, with dilution ratios of 0, 16 and 19. The results show that the film with the dilution ratio of 19 was a mixture of microcrystalline and amorphous material, while the others were amorphous.

2.1.3 Effect of Electrode Distance

We changed the interelectrode electrode distance to ~0.9 cm in the i-layer chamber to deposit low band gap material. From our experience, shorter electrode distances produces low band gap material.

After substantial experimenting with deposition conditions, we produced some low band gap materials (band gap = 1.72 eV). The film had a photoconductivity of 8.1×10^{-5} Scm^{-1} and a dark conductivity of 7.5×10^{-11} Scm^{-1}. However, the γs were low (~0.7). The devices fabricated with this material showed a low fill factor and efficiency.

V_{oc}	J_{sc}	FF	Eff
0.745 V	12.57 mA/cm^2	0.622	5.83%

The low γs of the film and low fill factor of the device suggests that the material quality was not good. In addition, the uniformity of the film was poor.

2.2 DEVICE FABRICATION

2.2.1 Low Temperature Device

Devices were fabricated at low substrate-temperatures for use as the top cell of dual-junction cells. These cells have 2000Å thick i-layers, deposited at substrate temperatures of 120°C to 200°C. As we expected, V_{oc} goes down and J_{sc} goes up with increasing substrate temperature. The efficiency is between 6.9% and 7.6%. Light soaking experiments have been done to study the stability vs. deposition temperature (and hydrogen

content).

One important issue for the top cell is the V_{oc} drop vs. the thickness. Figure 5 shows the V_{oc} and the fill factor under red (FFr) and blue (FFb) filters vs. the thickness of the intrinsic layer. From the figure, it is clear that V_{oc} drops with decreasing cell thickness. Usually the fill factor under blue filter indicates the quality of the interface and layers near the interface, while the red fill factor indicates the quality of the bulk i-layer. From the figure, both FFb and FFr decrease when the thickness of the cell decreases. We think this fact is related to initial growth of the intrinsic layer. We plan to address the problem by improving the TCO morphology and the surface mobility of the precursor.

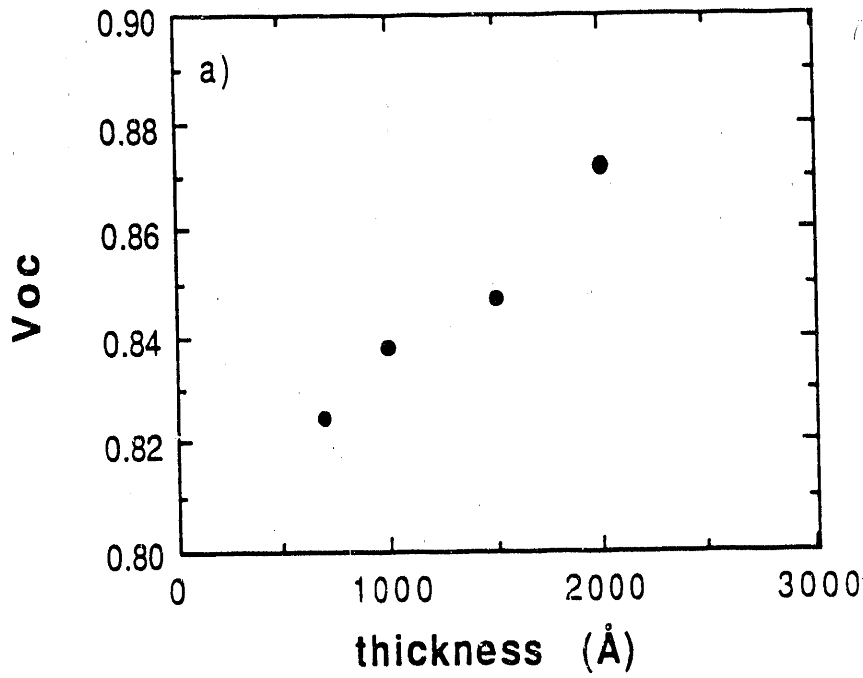

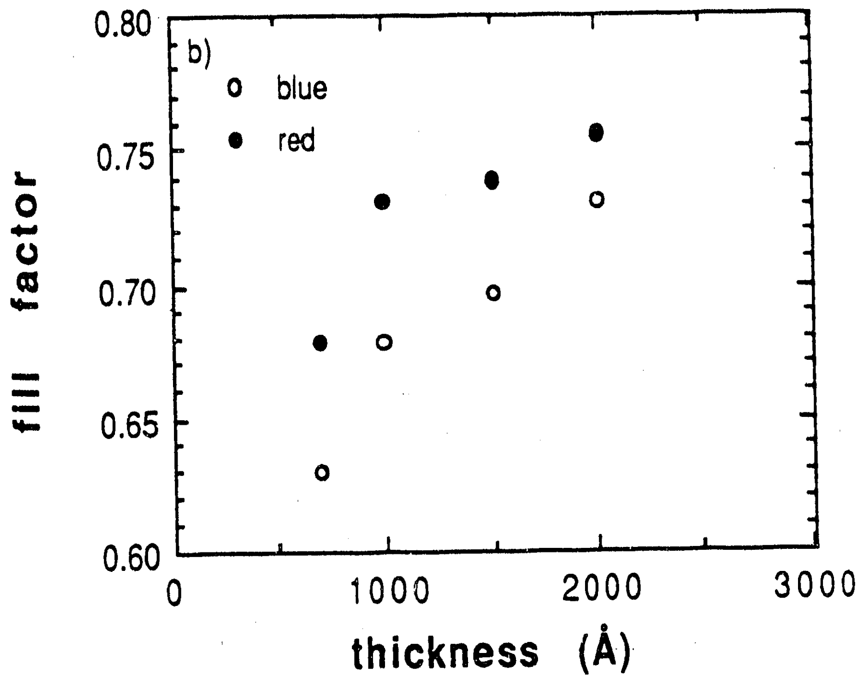

Figure 5. The photovoltaic parameters vs. the thickness of the intrinsic layer

2.2.2 High Temperature Device

Since both our high temperature i- and p-layers look promising, we fabricated single-junction devices using both high temperature p- and i-layers.

The device performance was poor, with the following photovoltaic parameters:

V_{oc}	J_{sc}	FF	Eff
0.625V	11.6 $mAcm^{-2}$	0.40	2.90%

To gain understanding of the poor performance, we measured the quantum efficiency (QE). Figure 6 shows the ratio of biased QE(-3V) to QE(0V). From the figure, it seems that the interface region as well as the region near the interface has a problem.

To determine whether the TCO changed during high temperature p-layer deposition, we deposited a single-junction device with a high temperature (300°C) p-layer and with a normal temperature (200°C) i-layer. The photovoltaic parameters were as follows:

V_{oc}	J_{sc}	FF	Eff
0.770V	14.7 $mAcm^{-2}$	0.699	7.94%

Although the V_{oc} is low, the performance is substantially different from the previously described device. Thus, we conclude that damage from the higher temperature to the TCO is NOT the major cause for the inferior cell performance. The problem appears to be diffusion of impurities into the i-layer.

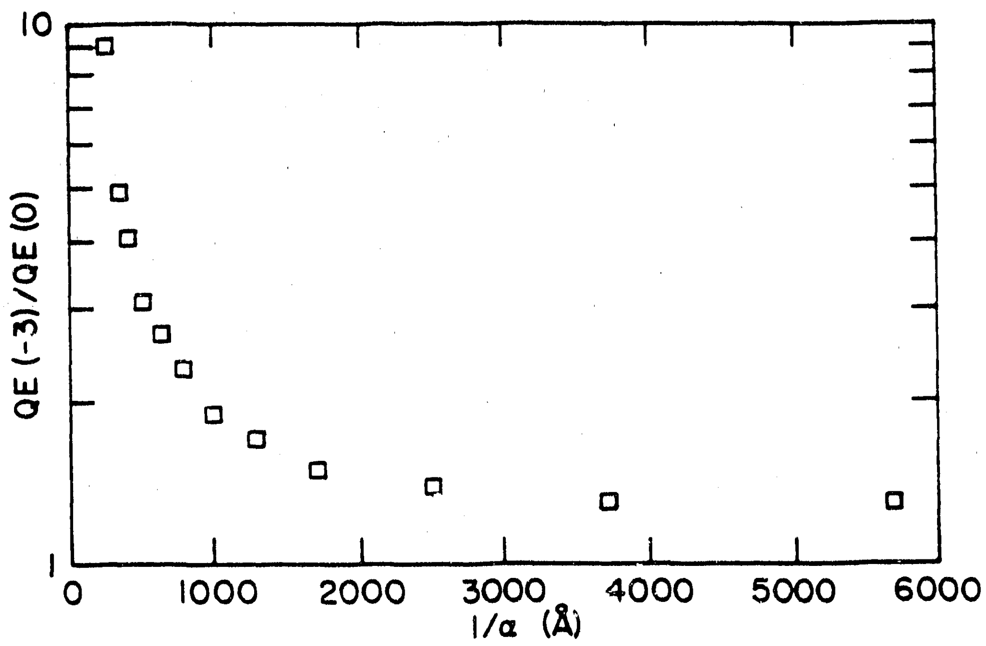

Figure 6. The biased quantum efficiency.

To block any diffusion from the p-layer, we deposited various conducting metal oxides (TiOx, NbOx, TaOx) and a-SiC:H between the p- and i-layers. The cells coated with metal oxides have very low efficiencies, probably due to improper band gap alignment. The cell coated with a-SiC:H had a slightly better performance:

V_{oc}	J_{sc}	FF	Eff
0.599V	12.84 $mAcm^{-2}$	0.487	3.75%

We also deposited dual-juction cells with normal deposition temperature p-i-n layers in the top cell and high temperature p- and i-layers in the bottom cell, to see whether the high temperature process in the bottom cell affects the top cell. Again the performance was poor:

V_{oc}	J_{sc}	FF	Eff
1.14V	4.71 $mAcm^{-2}$	0.515	2.78%

Figure 7 shows the QE of the top cell (with the bottom cell flooded by a red bias light). For reference, QE of a device with normal temperature i-layer as the bottom cell is included. Note the big difference between these two top cells. We conclude that it is most likely that something has diffused into the i-layer at high deposition temperature. SIMS analysis was carried out and the result confirms this point. Boron was found in the entire i-layer for the devices fabricated at high temperatures.

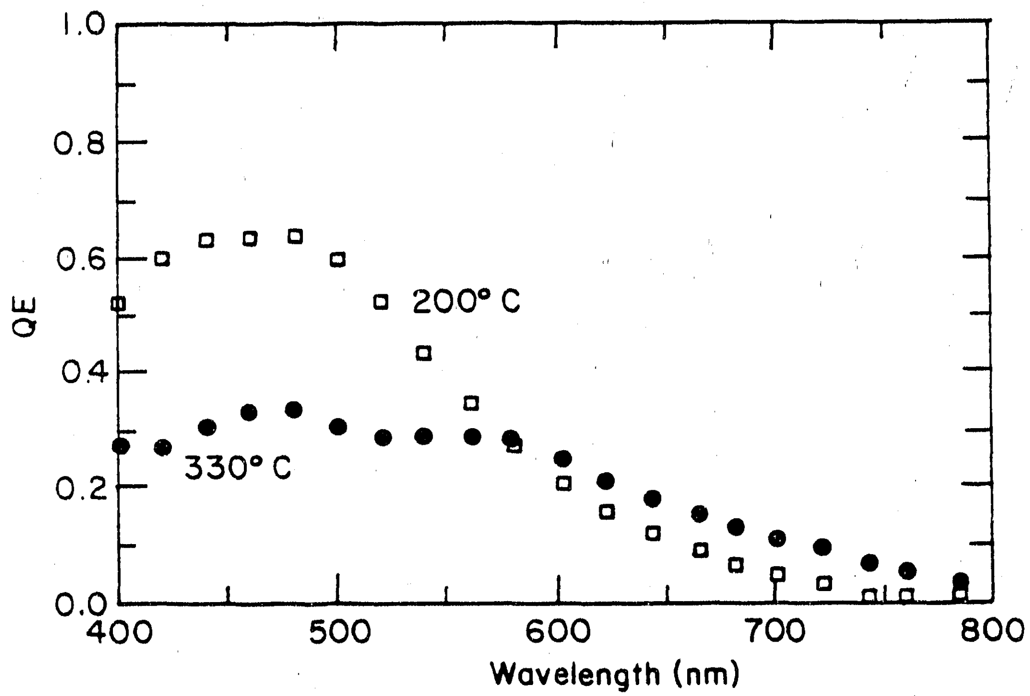

Figure 7. The quantum efficiency of a tandem device.

2.2.3 N-I-P Devices with High Temperature I-Layer

It was thought that the diffusion problem might not be as severe in a n-i-p structure. We fabricated two devices with n-i-p structure, one with i-layer deposited at 200°C and the other at 330°C. The cells have a structure of glass/TCO/a-n+/i/a-p/ITO. The doped layers were all deposited at 200°C. Although this structure results in a low fill factor due to the high series resistance of the contact (no metal contact was used), it is still good for comparison. Table 1 lists the photovoltaic parameters of these two cells:

Table 1 Photovoltaic Parameters of n-i-p cells

Run#	V_{oc} (V)	J_{sc} ($mAcm^{-2}$)	FF	Eff (%)	Deposition Temp. (°C)
710	0.778	9.48	0.576	4.25	200
711	0.624	8.46	0.303	1.64	330

From Table 1, it is obvious that the device performance varies with different i-layer process temperatures, most likely due to phosphorous diffusion. Thus, we conclude that dopant diffusion will be a severe problem for a high i-layer process temperature.

2.2.4 Devices With i-layer Deposited With Hydrogen Dilution

Utilizing a high frequency plasma (110 MHz) with heavy hydrogen dilution we produced microcrystalline intrinsic layers with large apparent band gaps. The Tauc band gaps of intrinsic layers deposited on Corning 7059 glass ranged from 1.8 to 2.1 eV, although the higher bandgap, microcrystalline material might be different when grown on TCO due to the importance of nucleation in the growth of microcrystalline material. Solar cells were produced with instrinsic layers having a range of hydrogen dilutions. The p-i-n solar cells fabricated all used the same a-SiC p-layer with a graded a-SiC buffer layer and our standard a-Si n-layer. The intrinsic layers were approximately 2000Å thick.

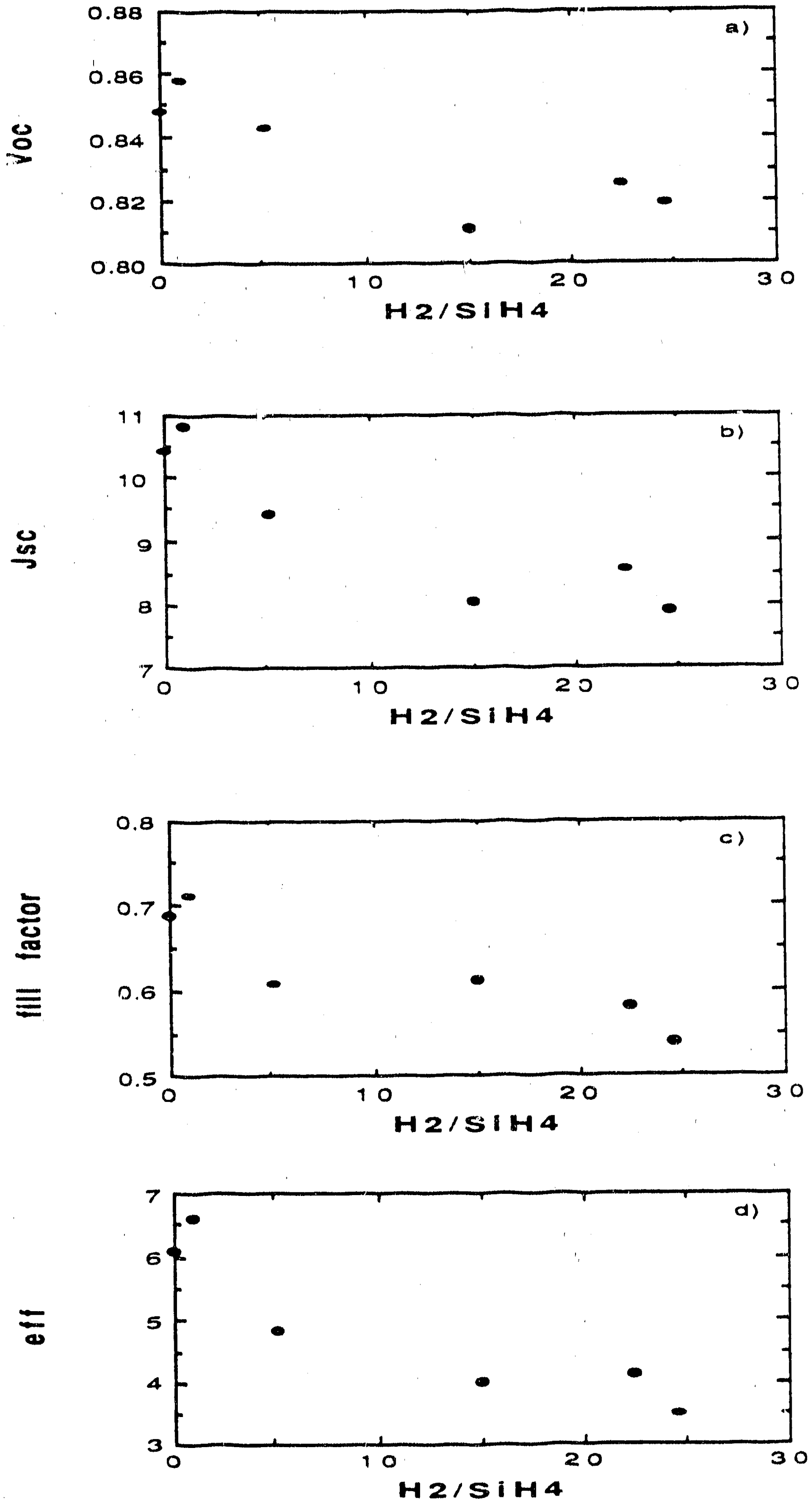

Figure 8. The photovoltaic parameters vs. the hydrogen dilution

The initial photovoltaic properties are shown in Figure 8 as a function of the H_2/SiH_4 mass flow ratio. The best performance in this series occurs for a ratio of 1, being slightly better than that for pure silane. All of the photovoltaic properties show a monotonic decrease with increasing hydrogen content above a ratio of 1. The decrease in short-circuit current is easily explained by the lower absorption at higher hydrogen dilutions. Interestingly, the open circuit voltage decreases even though the intrinsic layer bandgap increases. The blue current increases slightly as the hydrogen dilution increases, suggesting that some etching of the p/buffer layer occurs during the initial period of deposition of the intrinsic layer. Additionally, the blue fill factor is relatively low for all devices which generally indicates a poor p-i interface. The red fill factor drops in the same way as the AM1.5 fill factor.

2.3 STABILITY

2.3.1 Long Term Stability of Dual-Junction Cells

We finished a long term (2000 hrs) stability study of the dual-junction cells. This study is a continuation from the previous high-deposition-rate project. There are two purposes for this study: firstly, we want to see whether the degradation saturates after very long time light soaking. Secondly, to compare the stability of low-deposition-rate material from SiH_4 with high-deposition-rate material from Si_2H_6.

The cells involved have low-deposition-rate i-layers from SiH_4 and high-deposition-rate i-layers from SiH_6. Unfortunately, all the cells with Si_2H_6/SiH_4 as top/bottom cells shorted after ~450 hours of light soaking. Figure 9 shows the degradation of the normalized efficiencies for the SiH_4/SiH_4, SiH_4/Si_2H_6 and Si_2H_6/Si_2H_6 cells.

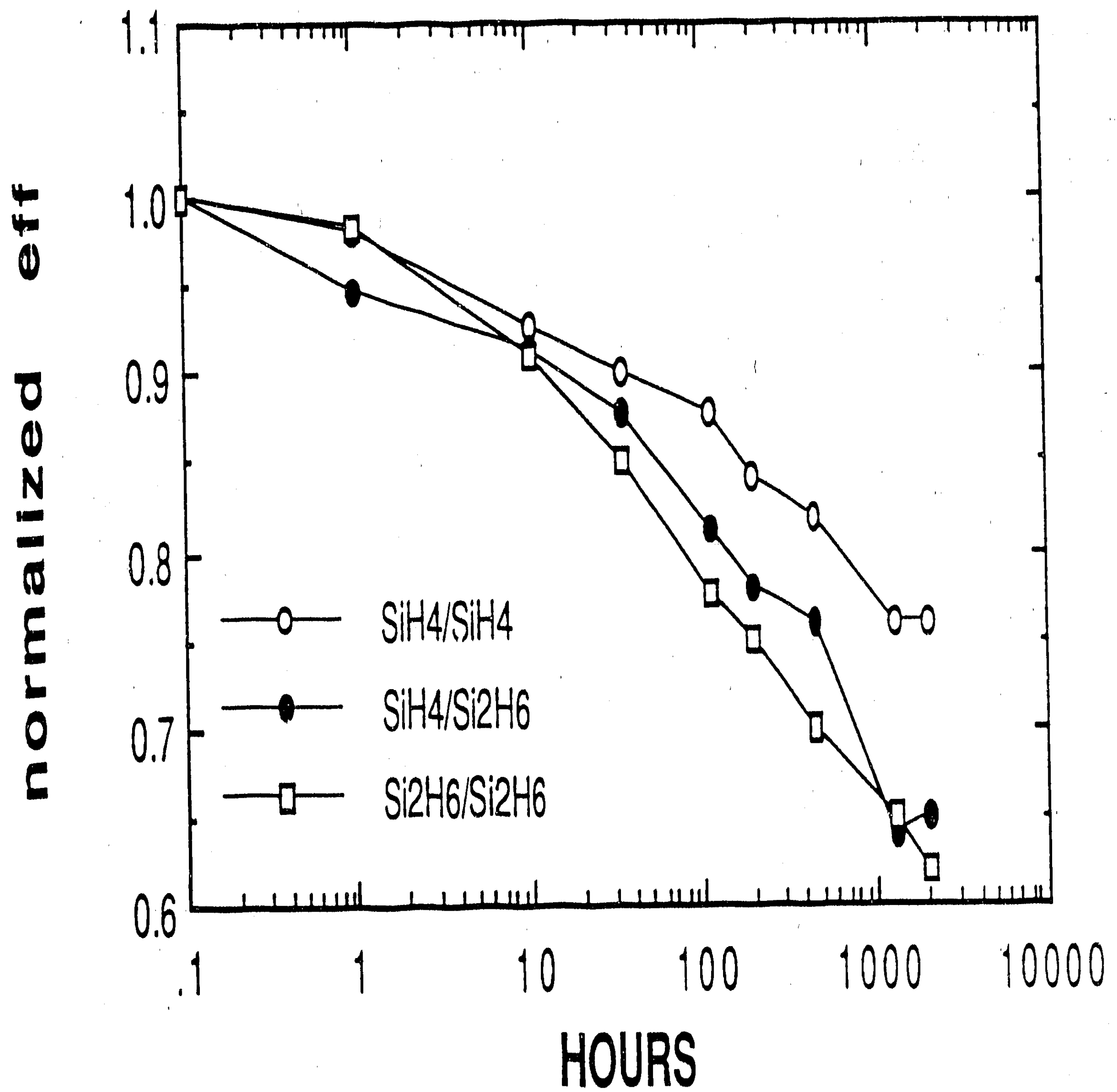

Figure 9. The normalized efficiency vs. the light soaking time

Table 2 lists the details of the initial and final photovoltaic parameters.

Table 2 Light soaking effect on the dual-junction cells

		SiH_4/SiH_4	SiH_4/Si_2H_6	Si_2H_6/Si_2H_6
V_{oc}	initial	1.67	1.61	1.63
	final	1.62	1.56	1.57
	% drop	3%	3%	4%
J_{sc}	initial	7.20	7.10	7.06
	final	6.87	6.43	6.40
	% drop	5%	9%	9%
FF	initial	0.72	0.69	0.68
	final	0.61	0.52	0.48
	% drop	15%	25%	29%
Eff	initial	8.64	7.82	7.78
	final	6.81	5.22	4.82
	% drop	21%	33%	38%

There are several interesting points we would like to make:

a) It appears that the efficiency of the SiH_4/SiH_4 and SiH_4/Si_2H_6 cells stabilized after 1300 hours of light soaking while the Si_2H_6/Si_2H_6 cells did not. The saturated efficiency the of SiH_4/SiH_4 dual-junction cell is 6.8%.

b) Although we need more data to confirm whether saturation really occurred, it is clear that before 1000 hours, the degradation is linear with the logarithm of soaking time.

c) The slope of the degradation depends on the i-layer material. The cells with Si_2H_6 high-deposition-rate i-layers are inferior.

d) As we expected, most of the drop is in FF.

2.3.2 Stability vs. Deposition Conditions

Usually the i-layer deposition conditions are optimized for the highest initial efficiency. Whether these conditions also give the highest stable efficiency is not clear. We fabricated a group of samples, systematically changing the intrinsic layer deposition conditions. The thickness of the i-layer of the samples was 3500Å, the temperature varied from 187°C to 213°C, the RF power from 3W to 5W, and the pressure from 600 mTorr to 800 mTorr.

Since the parameter variation is relatively small, the initial performances are within a narrow range and show a broad peak at the optimized point. The average efficiency of these samples with Ag back reflector is 8.8 ± 0.4% One interesting point is that the current density under blue illumination drops systematically with an increase of the RF power. We think this suggests the importance of the p/i interface. These cells have been light soaked.

Half of this group of samples has completed 600 hours of light soaking while the other half has passed 300 hours. The best efficiency after 300 hours soaking is 7.34% for an ITO/Ag device and 6.31% for an Ag device. Several devices exhibit crossover with cells having lower initial efficiencies having higher final efficiencies.

Table 3 Intrinsic Layer Deposition Conditions

Run #	670	671	672	673	674	675	676	677	678	679
Temperature (°C)	200	200	200	200	200	185	185	215	215	215
Pressure (mTorr)	700	600	700	800	700	600	700	600	700	700
Power (W/cm^2)	0.04	0.04	0.03	0.04	0.05	0.04	0.03	0.04	0.05	0.04

The efficiencies as a function of time are shown in Figure 10. The relative degradation after 300 hours ranges from 15% to 30% for the various runs. There is no indication of saturation of the efficiencies after 600 hours of light soaking. The degradation in efficiency of these samples is generally not linear with log(time), but drops somewhat faster. The normalized V_{oc}, J_{sc}, and fill factor are shown in Figures 11, 12 and 13. The open-circuit voltage remains essentially constant for light soaking times of about 30 hours and then begins to degrade logarithmically with time. Degradation of the open-circuit voltage constitute 3-5% of the total degradation. The delayed degradation of V_{oc} largely accounts for the curvature in the efficiency degradation. The fill factor exhibits a simple logarithmic drop with time over the entire time range, neglecting the initial value which was arbitrarily put at 0.1 hour.

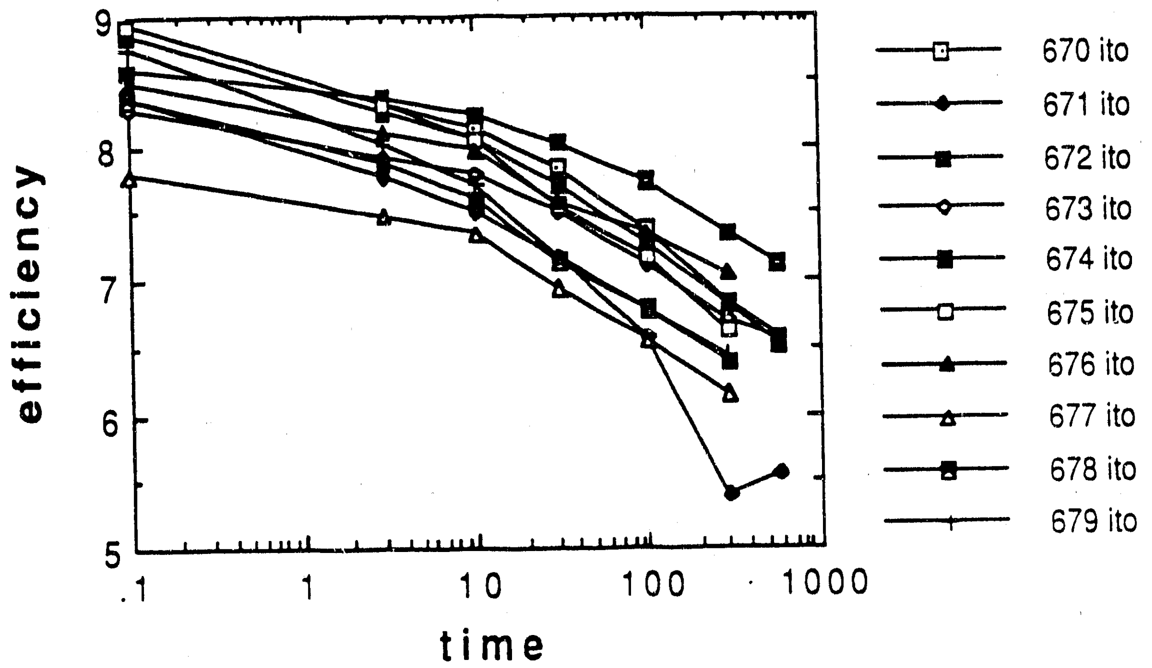

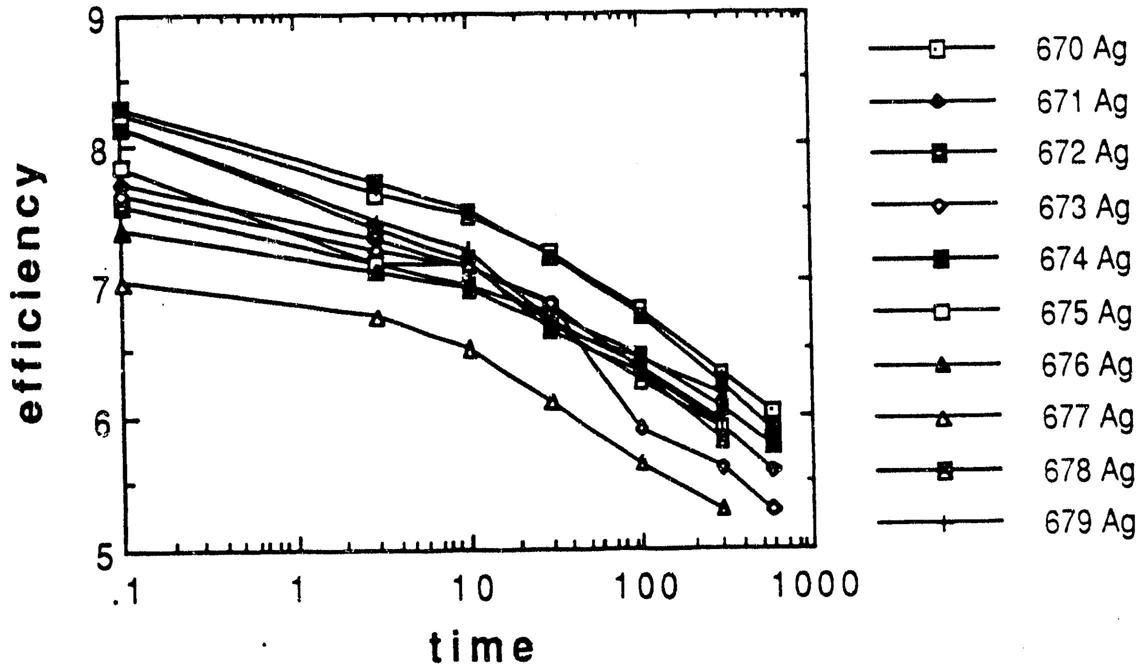

Figure 10. The efficiency vs. the light soaking time

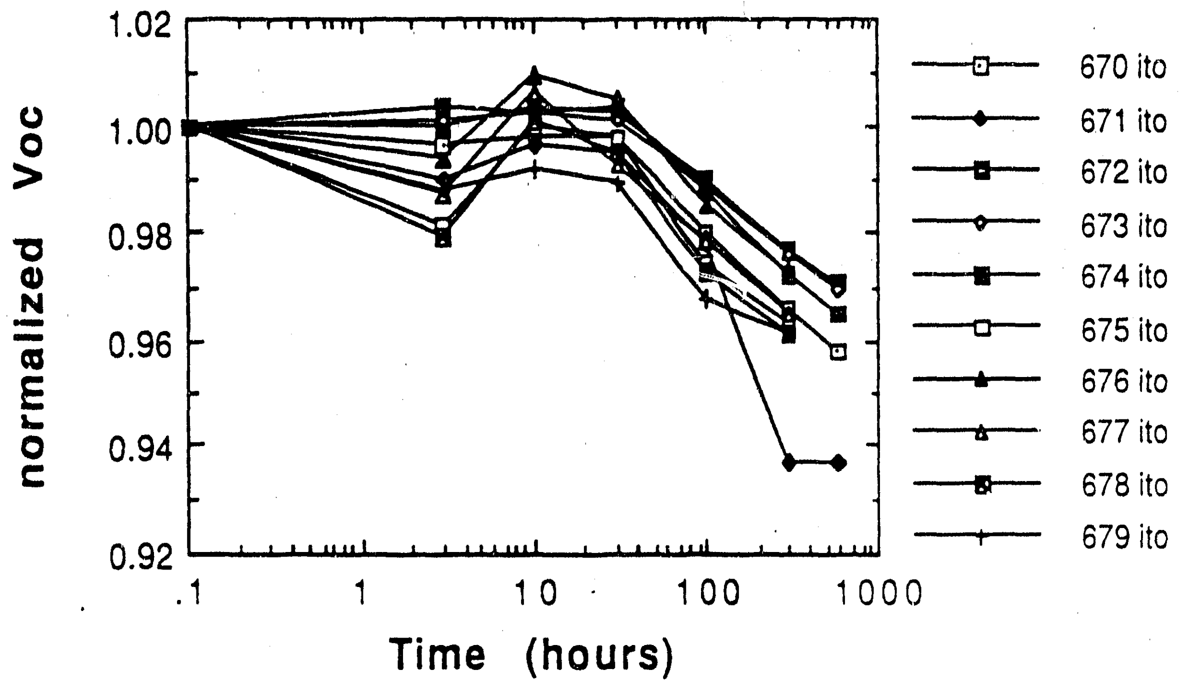

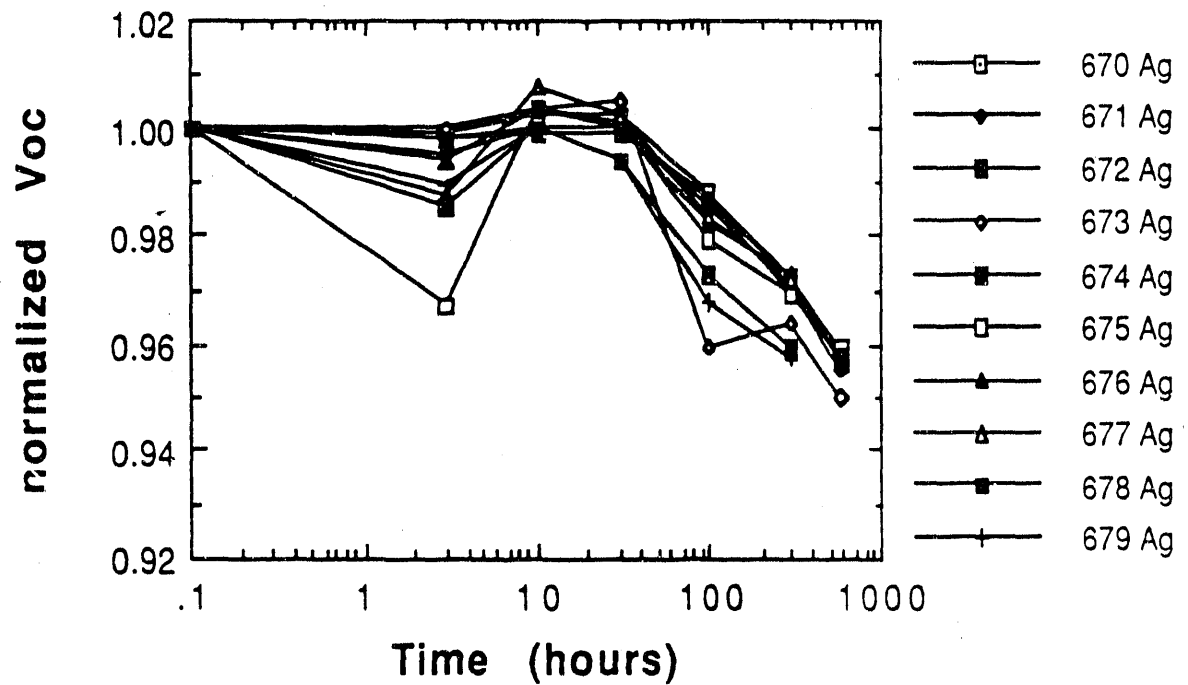

Figure 11. The normalized open circuit voltage vs. the light soaking time

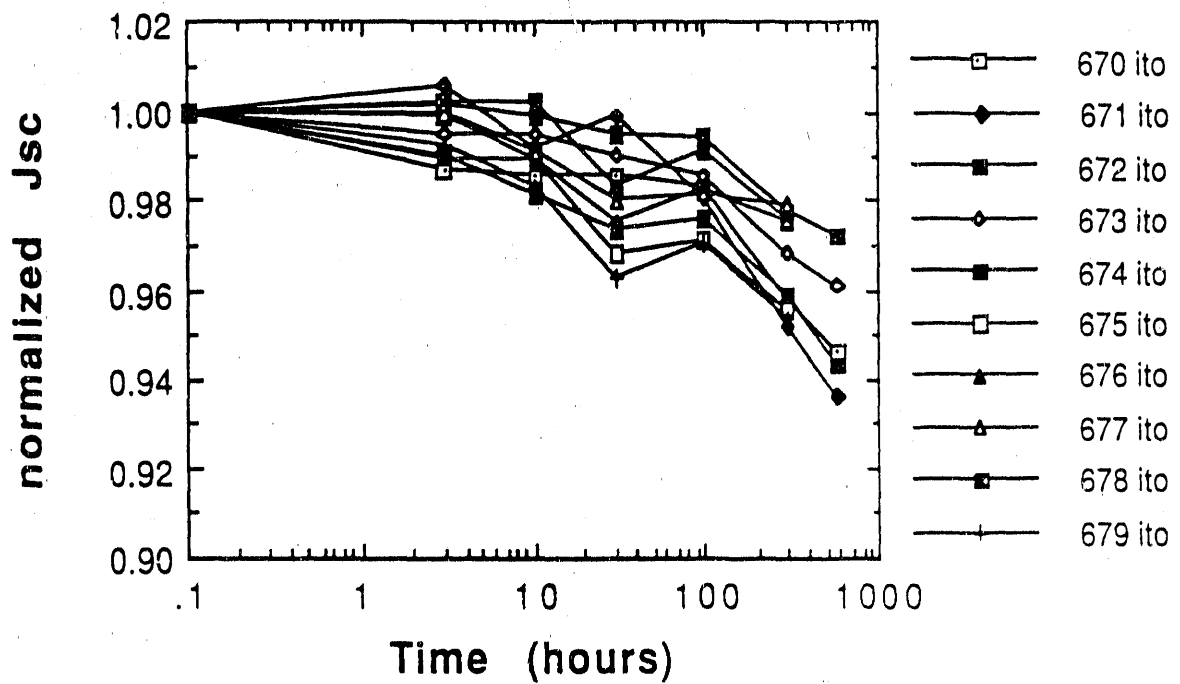

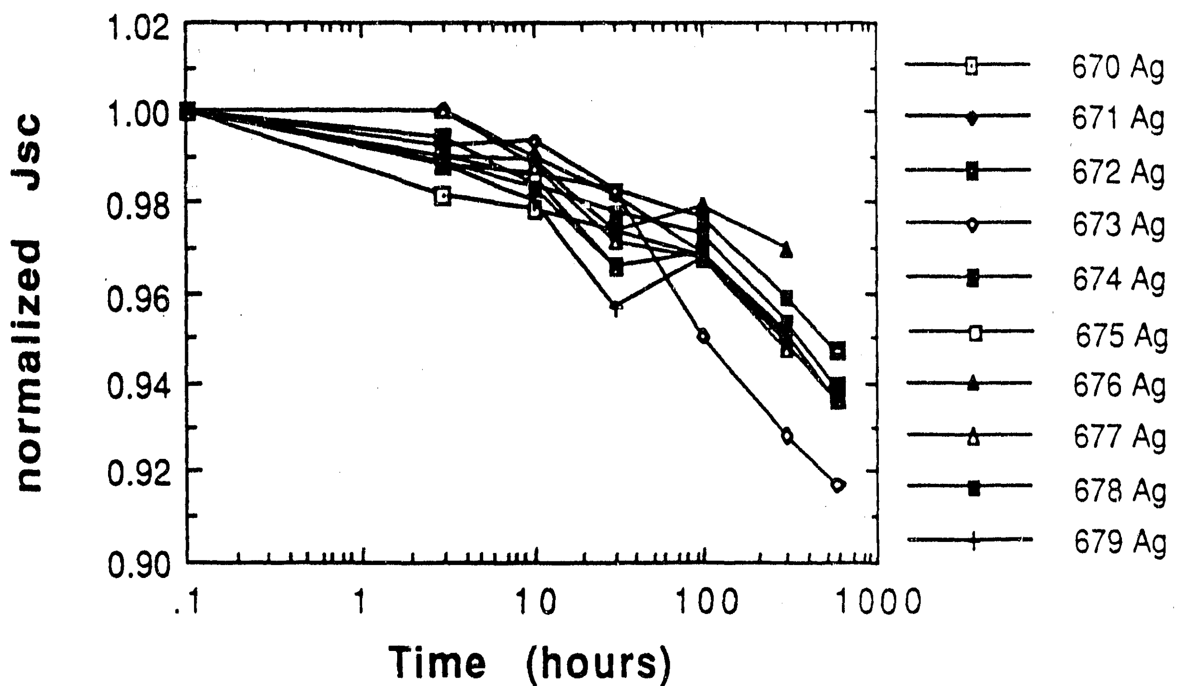

Figure 12. The normalized short circuit current density vs. the light soaking time

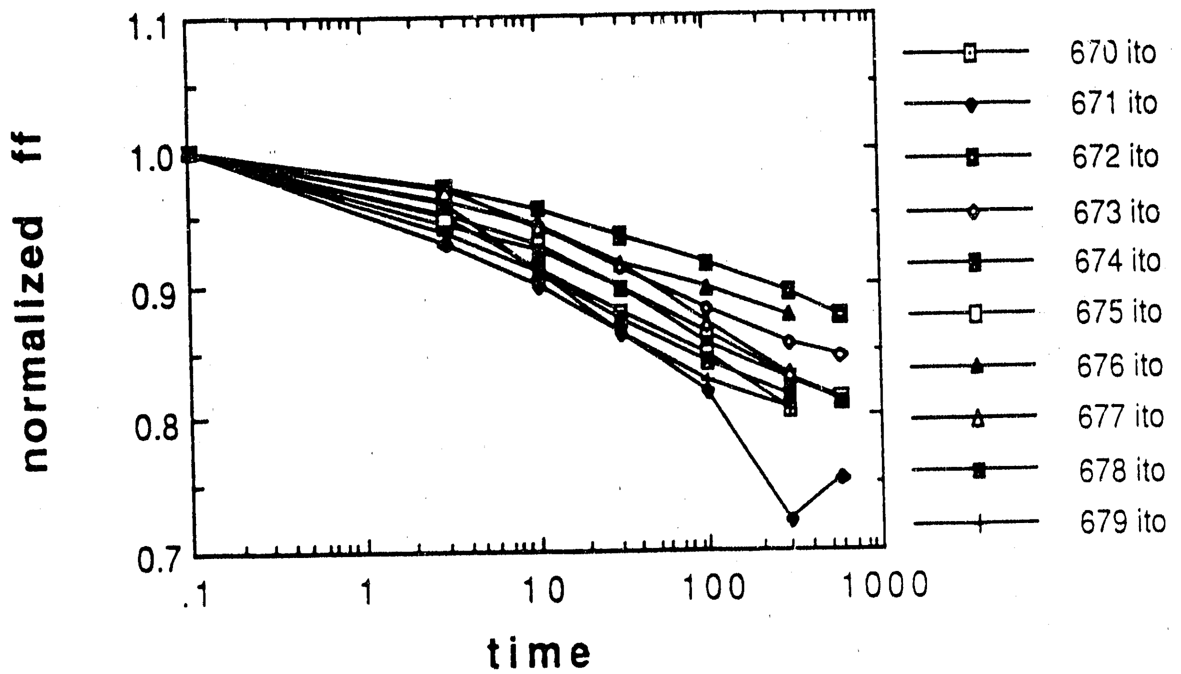

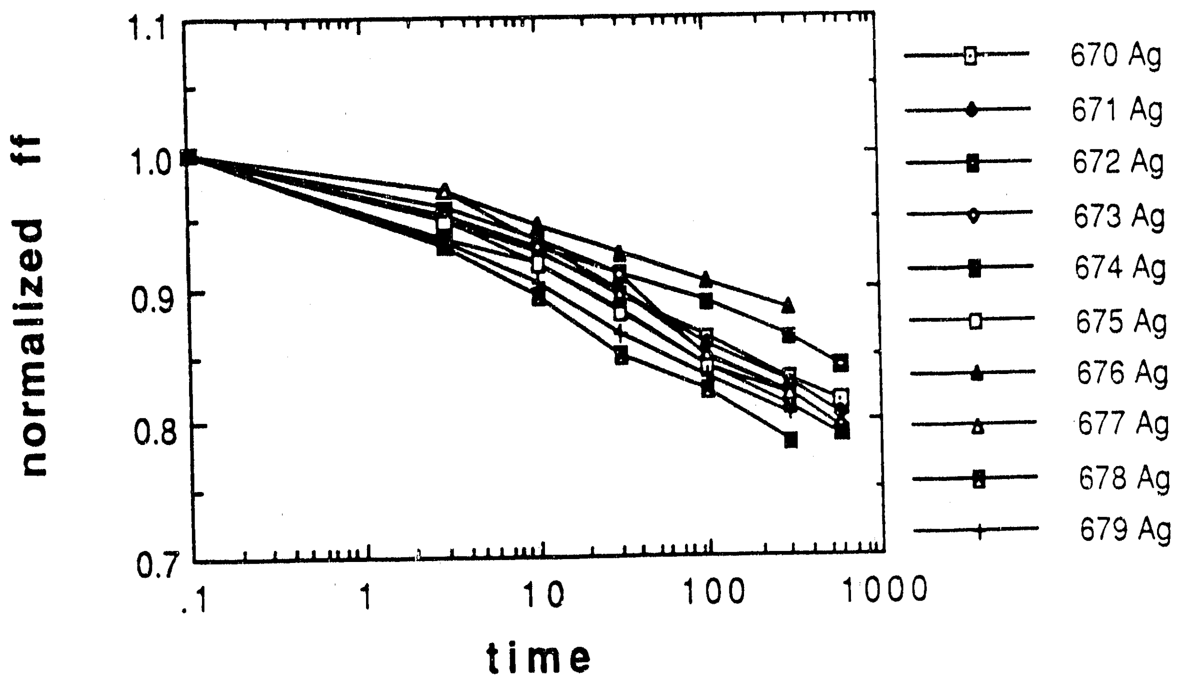

Figure 13. The normalized fill factor vs. the light soaking time

In this series of devices, the rf power, pressure and temperature of the intrinsic layer were varied around the optimum point. The initial efficiency shows a weak dependence on pressure with a weak optimum at 700 mTorr. Pressure variations had little effect on the efficiency after 300 hours of light soaking.

Figure 14 shows the efficiency of the devices as-deposited and after 300 hours of light soaking as a function of rf power. The initial efficiency increases slightly with increasing power. These devices show a clear trend toward better stability at lower rf powers. The low power device with an ITO/Ag back contact shows both the lowest percent degradation (17%) as well as the highest final efficiency (7.11%) after 600 hours.

Figure 15 shows the initial and degraded efficiency of devices as a function of intrinsic layer deposition temperature. The temperature axis is a heater set temperature. The initial efficiency drops slightly with increasing temperature, probably due to a deterioration of the p-i interface. No obvious difference in degradation exists with temperature in this limited range.

The run-to-run variations in initial performance and in degradation might be attributable to thickness variations between the runs.

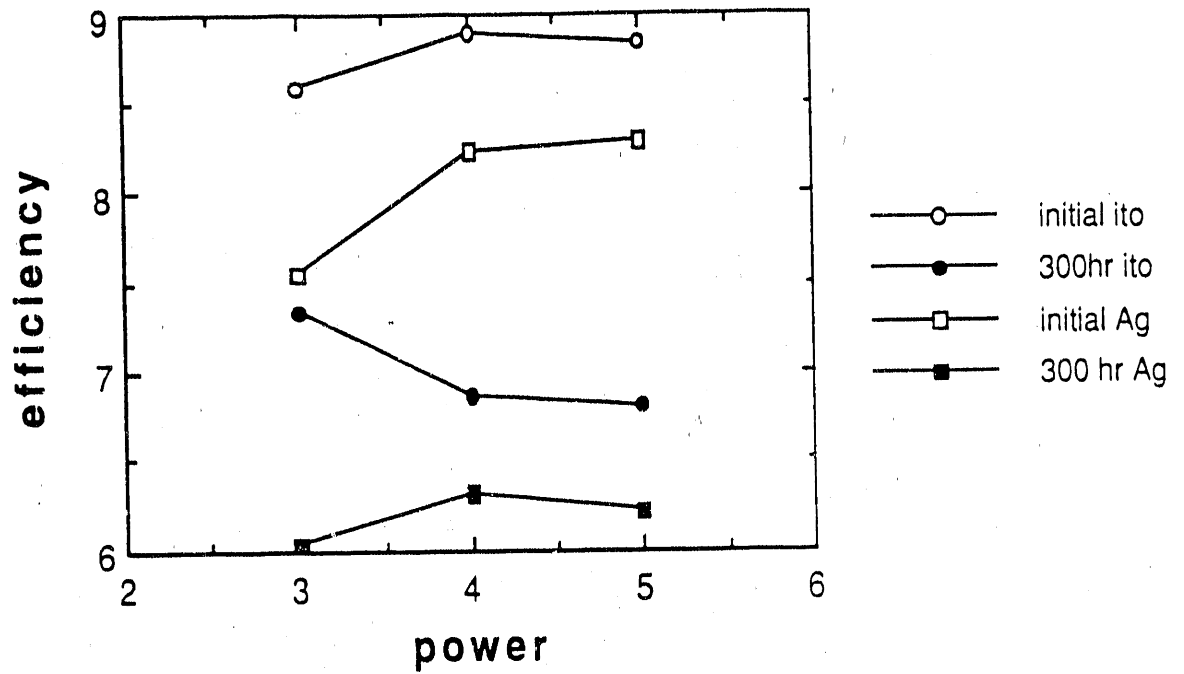

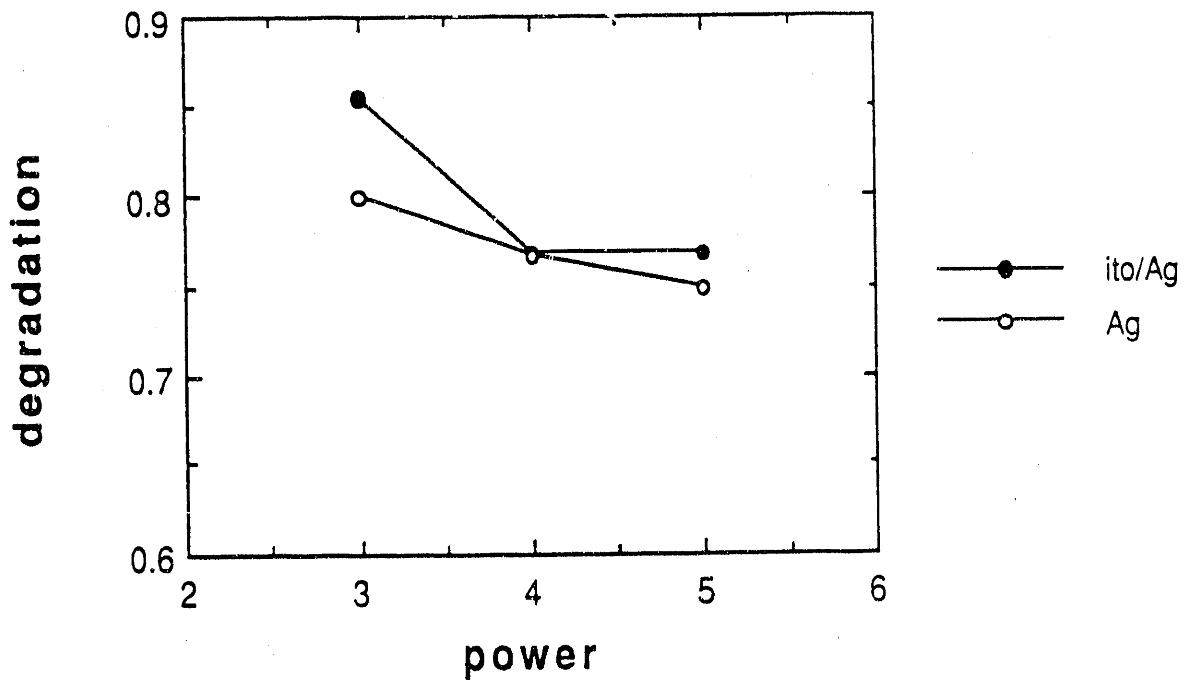

Figure 14. The efficiency vs. the r.f. power density

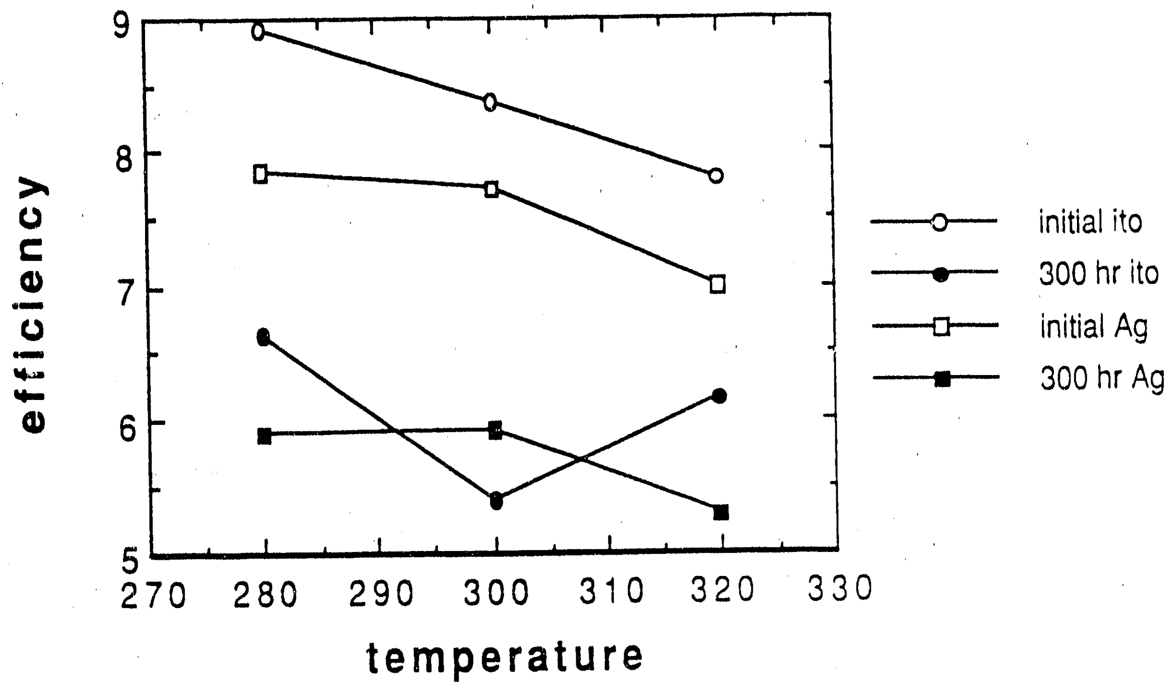

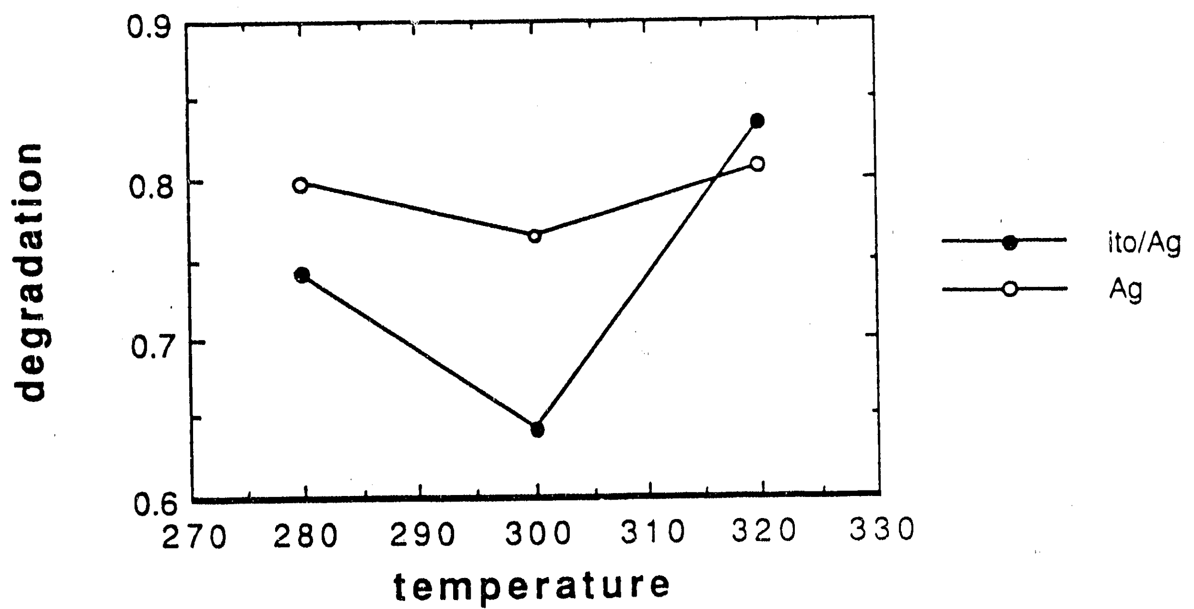

Figure 15. The efficiency vs. the deposition temperature

2.3.3 Stability vs. Deposition Temperature

This study is for clarifying the relationship between the degradation and hydrogen concentration in the film. To clarify the relationship between the i-layer property versus the device performance, i-layers were deposited at 120°C, 213°C, 230°C, 300°C, and 330°C and light soaked with the devices. Figures 16, 17, 18 and 19 show the light soaking data of the absolute photovoltaic parameters. The deposition temperatures of the i-layers of the devices are marked on the graph. Figure 20 shows the light soaking data of photoconductivity of the i-layers deposited at different temperatures. Figure 21 shows γs (where $\sigma_{ph} \sim G^{r}$, G is the photon generation rate) of some i-layers.

The devices with i-layers deposited at high temperature (330°C) had low initial efficiencies, due to boron diffusion. These cells look very stable during light soaking. However, even after 600 hours of light soaking, the absolute fill factor and efficiency of the high temperature cells are still much lower than the others. Thus we think that these cells look more stable because they started with a highly-defective material (e.g., high impurity in the i-layer). Note that the percentage drops of the fill factor (Figure 22) vs. deposition temperature remain constant within the temperature range of 140°C to 200°C, but increase for the very low substrate temperature (e.g., 120°C). Thus, in the regime of good initial solar cell efficiencies, there is no clear correlation of observed degradation with substrate temperature or hydrogen content.

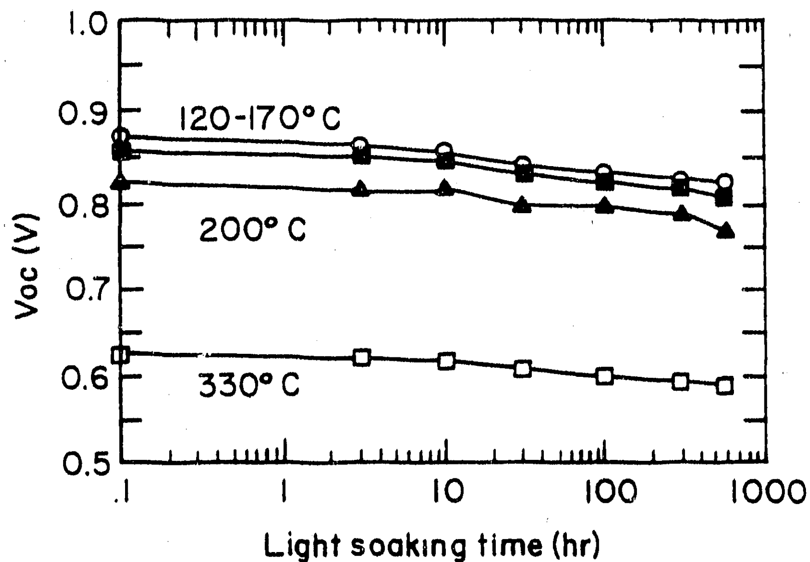

Figure 16. V_{oc} versus light soaking time. The i-layers of device were deposited at different temperatures, as marked on figure.

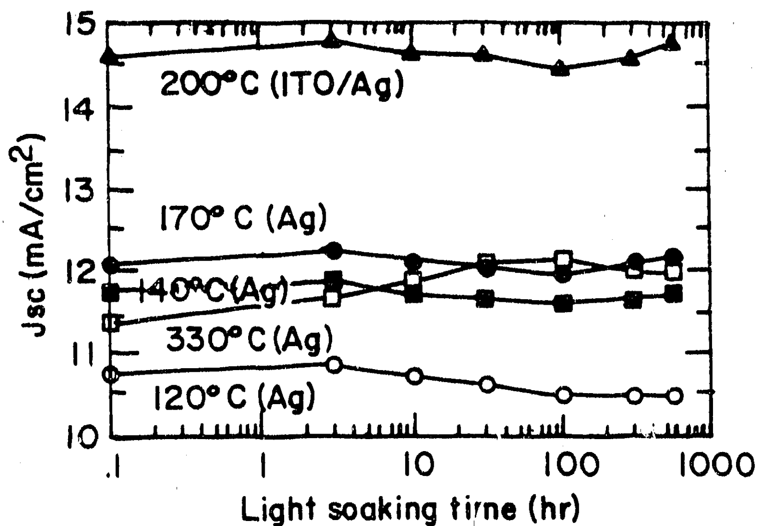

Figure 17. J_{sc} versus light soak time.

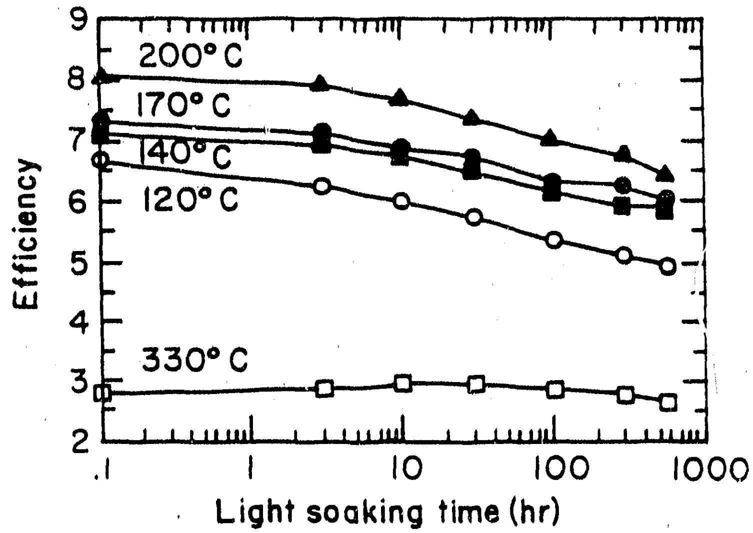

Figure 18. The fill factor versus the light soaking time. The symbols are the same as before.

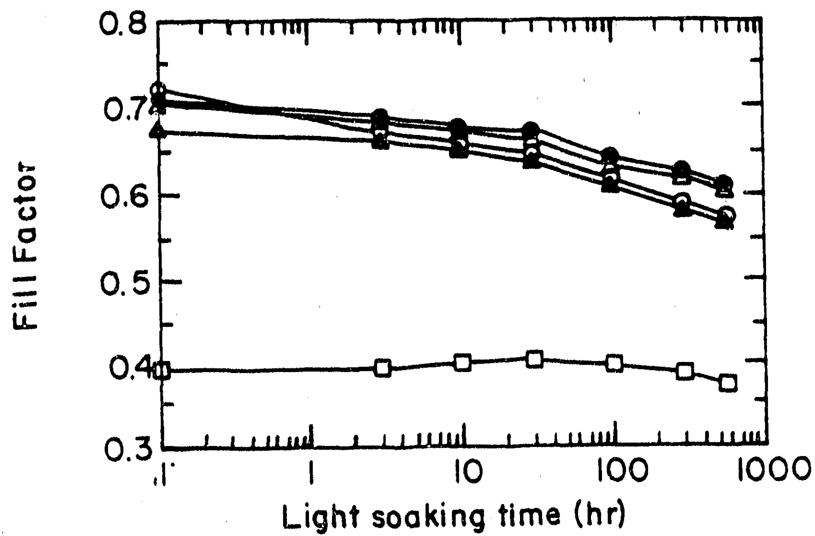

Figure 19. The efficiency versus the light soaking time. Note that the device which has 330°C i-layer is stable, but absolute efficiency is low.

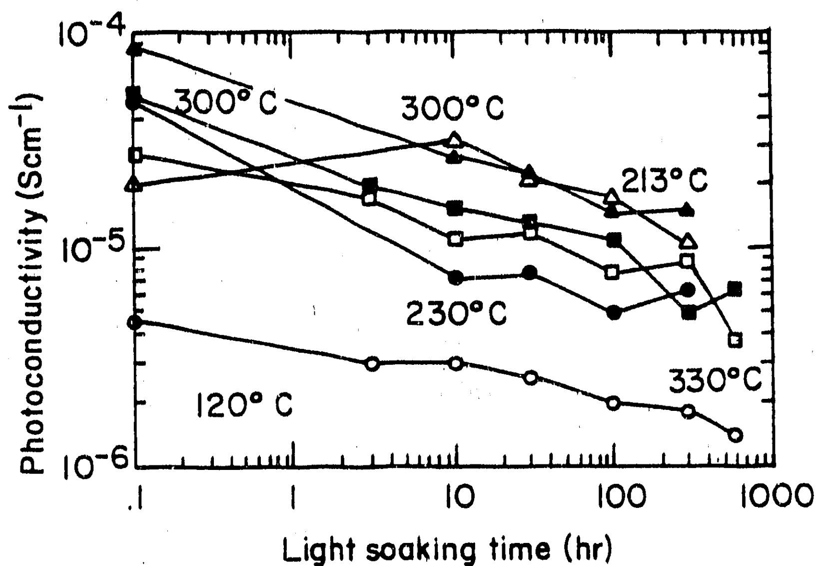

Figure 20. The photoconductivity of i-layers versus the light soaking time. Deposition temperatures are marked on the figure. Note that the photoconductivity of high temperature i-layers also drops.

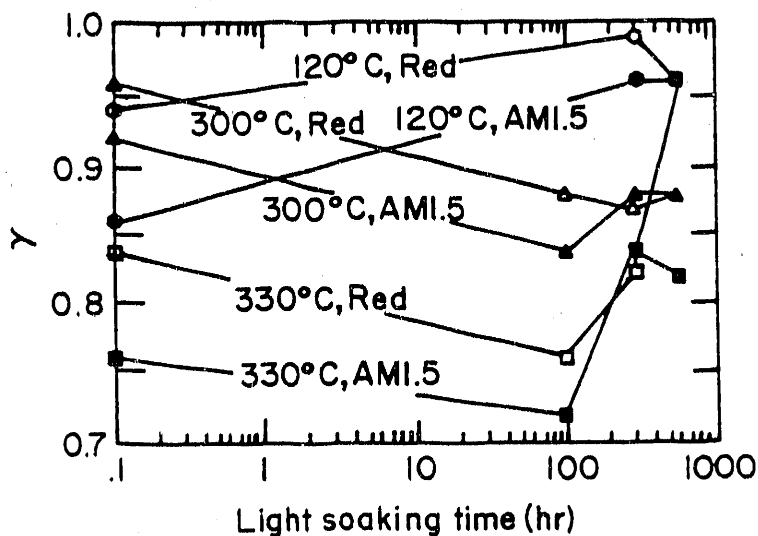

Figure 21. γ (where $\sigma_{ph} \propto G^{\gamma}$) versus light soaking time. Note that γs do not decrease.

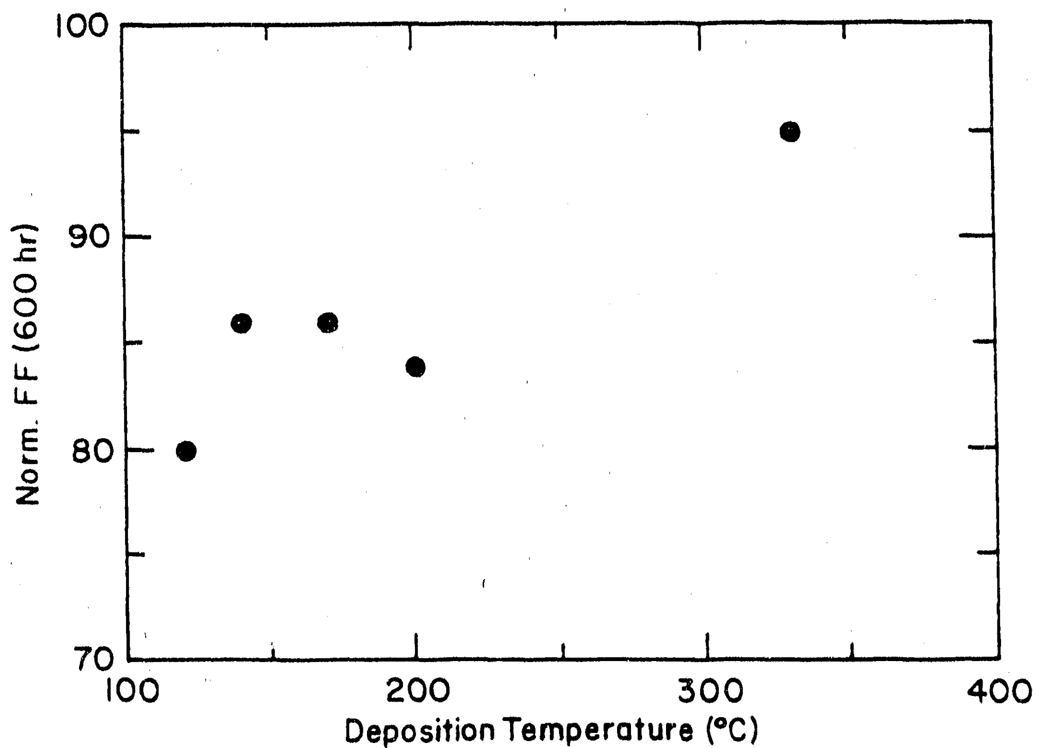

Figure 22. Normalized fill factor (after 600 hours light soaking) versus i-layer deposition temperature. Note that in certain temperature ranges, the normalized FF is constant.

Another interesting point is that both the photoconductivity of the film and the fill factor of the device have a severe drop at short light soaking times. However, the γs do not change much. Since the γs are measured under weak light, they reflect the density of states near the midgap. On the other hand, the photoconductivity is controlled by the total defect states between the dark Fermi level (Ef0) and quasi Fermi level (Efn).

$$\sigma_{ph} = q\mu n \qquad (1);$$

$$n = Gt = G/[V_{th}O \int_{E_{fo}}^{E_{fn}} N(E)\, dE] \qquad (2);$$

Here V_{th} is the thermal velocity of electrons, O is their capture cross section, and N(E) the density of states. γs change with N(E) (If N(E) is low, γs will be close to 1). Thus the fact that γs (weak light) do not change but σ_{ph}s (strong light) change suggests that the light induced states are close to the tail states, and might be D^{o}/D^{-} states. This is consistent with some other research group's observations.

2.3.4 Stability of the High Bandgap Cell

This study is for the top cells. The purpose is to see how the performance and stability change with cell thickness. The intrinsic layer thicknesses are in the 700Å to 2000Å range. Figure 23 shows the absolute efficiency versus light soaking time up to 600 hours. Figure 24 shows the normalized fill factor versus light soaking time. There is an additional 4-5% drop in efficiency due to degradation of the open-circuit voltage and short-circuit current. Figure 25 shows the efficiency before and after light soaking vs. cell thickness. From these figures, it is clear that the thinnest cell shows the lowest degradation. However, after 600 hours light soaking, the absolute efficiency of thin cells is still lower than that of the thicker cells. The efficiency of the 700Å cell (which is the thickness for the top cell) after soaking is close to 4%. The degradation is about 13%. The efficiency of the 2000Å cell after soaking is above 5%, approaching the first year target for high band gap single junction cells.

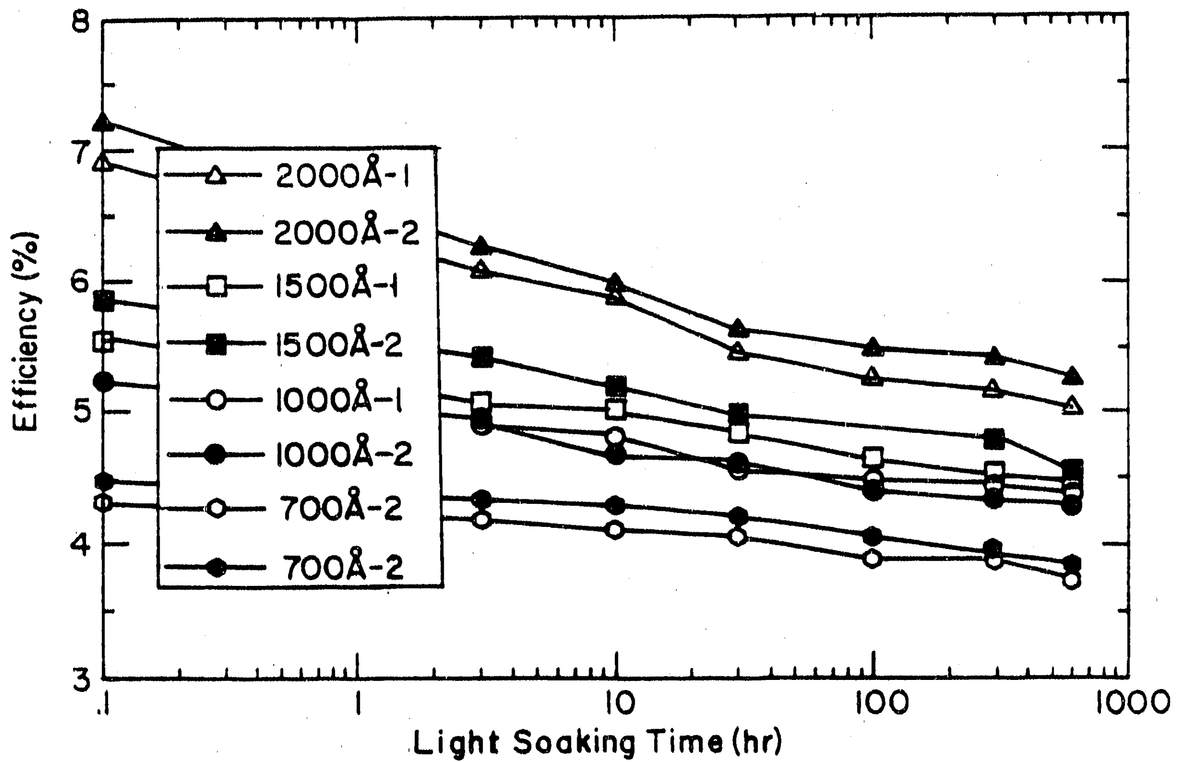

Figure 23. The efficiency versus light soaking time for devices with different i-layer thicknesses.

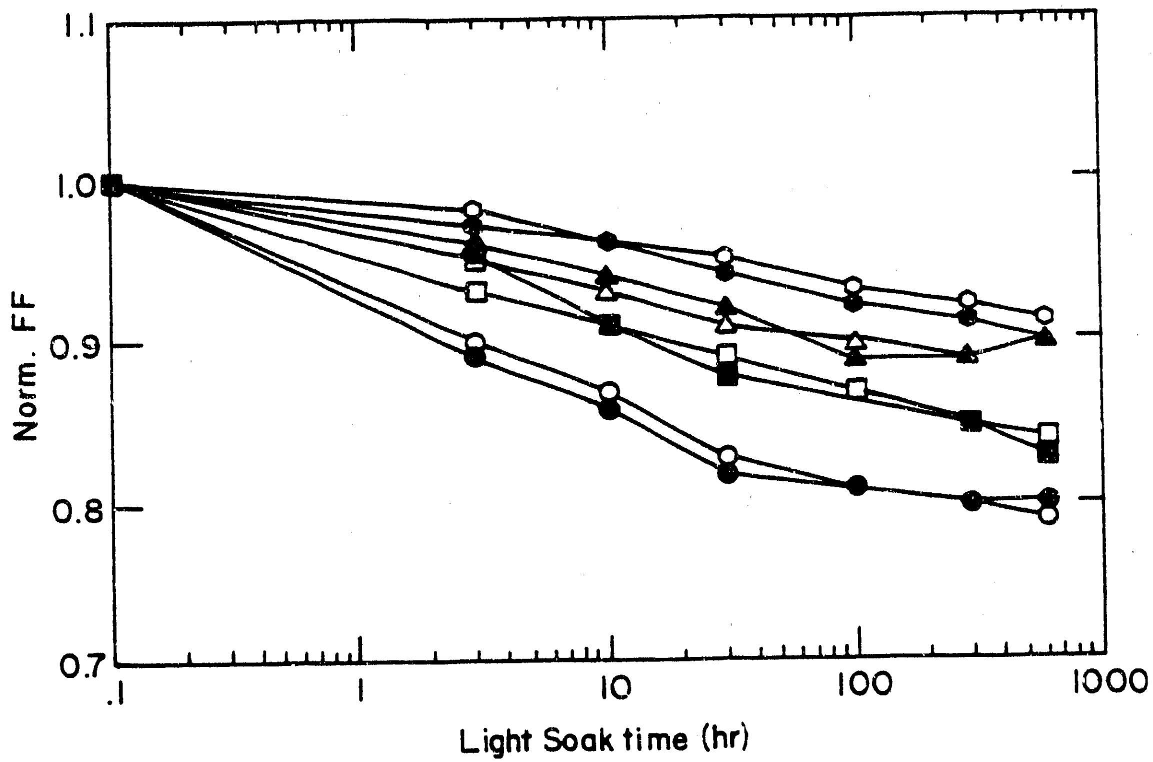

Figure 24. The normalized fill factor versus light soaking time for devices with different i-layer thicknesses.

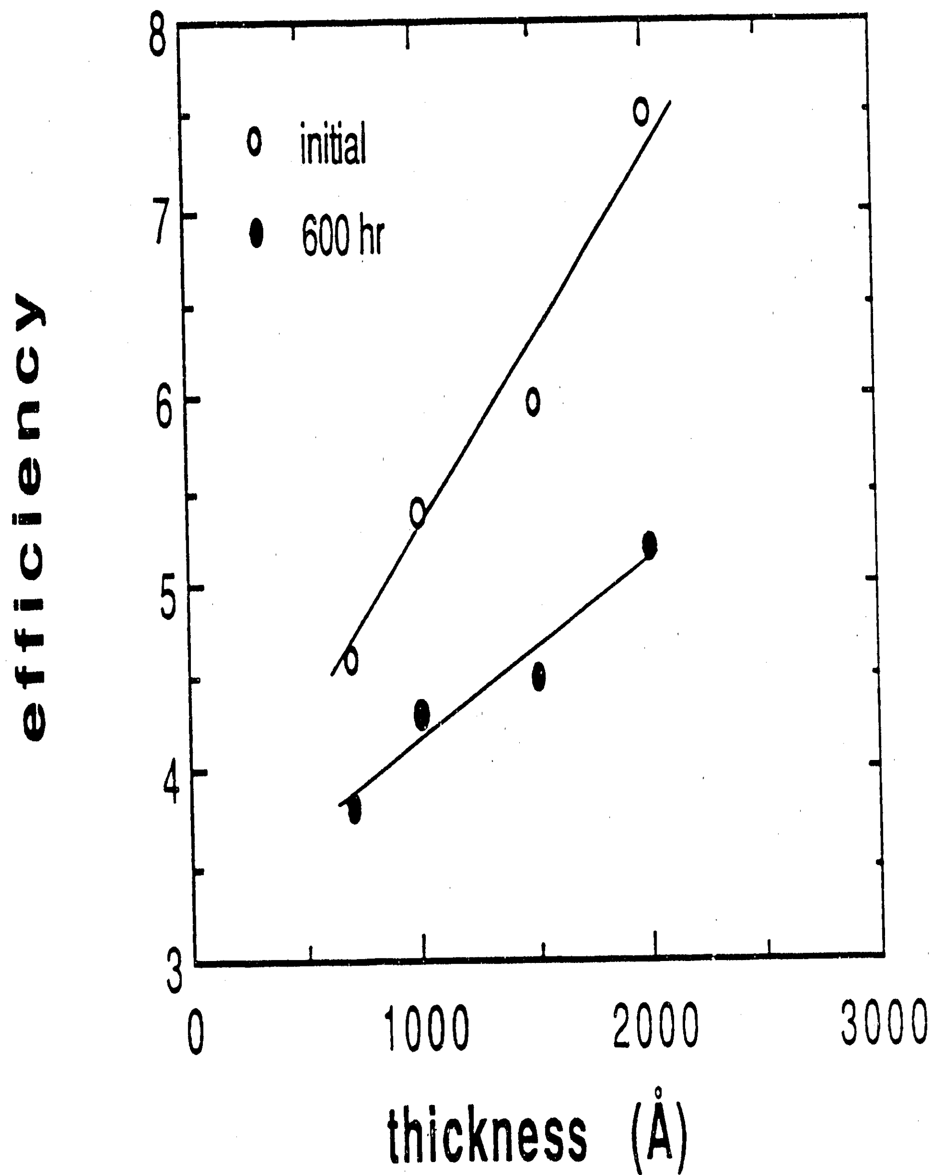

Figure 25. The initial and degraded efficiency versus the intrinsic layer thickness

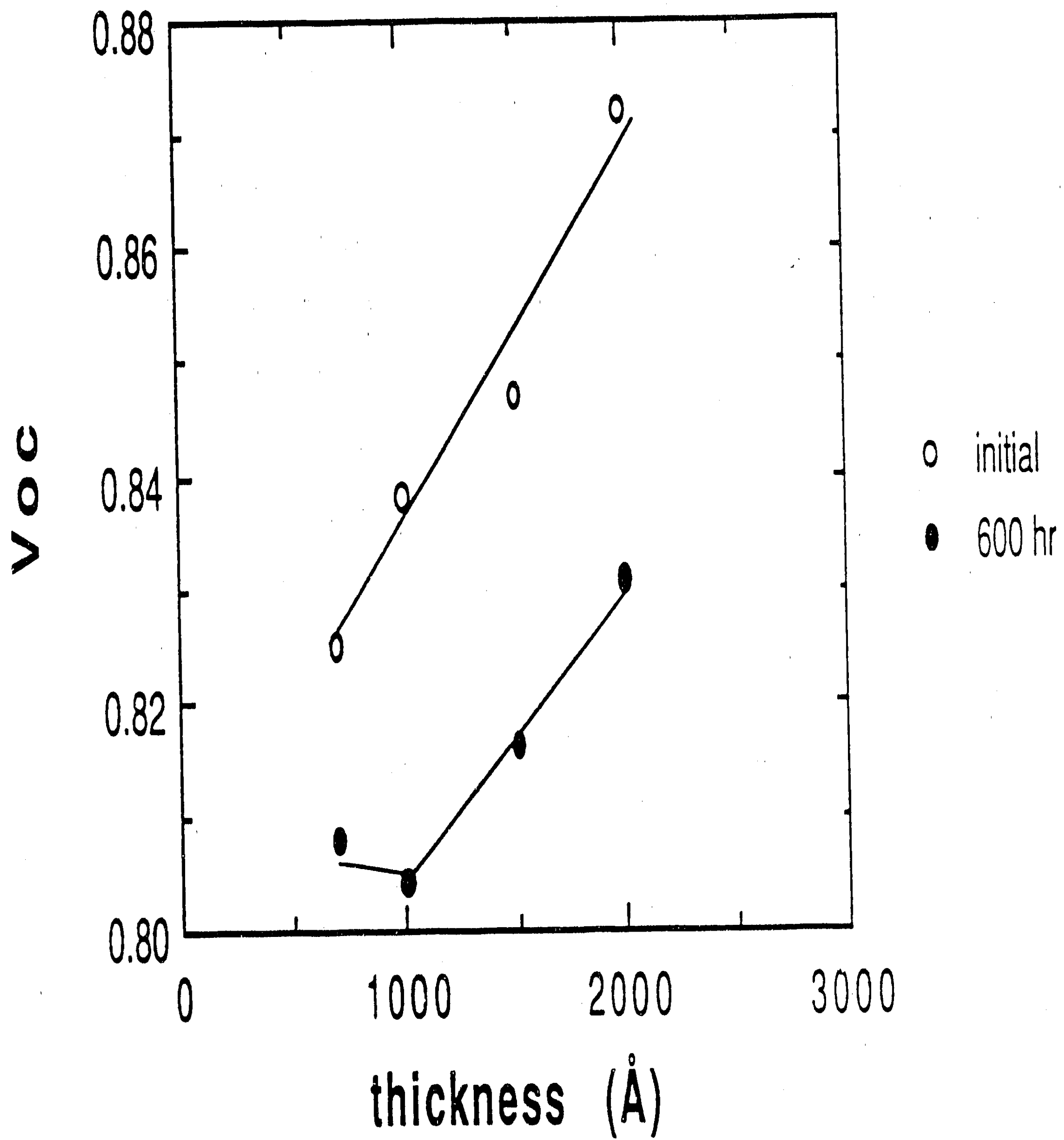

Figure 26. The initial and degraded open circuit voltage versus the intrinsic layer thickness

Figure 26 shows the V_{oc} vs. the cell thickness before and after light soaking. It appears that the V_{oc} degradation is lower for thin cells, which might be related to the recombination.

The major conclusion we can draw from this study is that the V_{oc} of the thin top cell needs to be improved (e.g. by improving TCO). Also the stability of the high band gap material needs to be improved.

2.3.5 Stability of the Cells with i-layers Deposited with H Dilution

The absolute and normalized efficiencies versus light soaking time are shown in Figure 27. The devices having intrinsic layers made with high hydrogen dilution show the best stability, having as little as 9% degradation after 844 hours of light soaking. The device made from pure silane exhibits a monotonic decrease in open-circuit voltage with light soaking while the hydrogen diluted devices show an initial increase in V_{oc} of as much as 40 mV and a constant value after that. There is no consistent variation of the final V_{oc} with hydrogen dilution. The short-circuit current of all devices decreases slightly with light soaking time, with the decrease being almost entirely in the blue end of the spectrum. The fill factors of all devices except the microcrystalline one converge to essentially the same value of about 0.57.

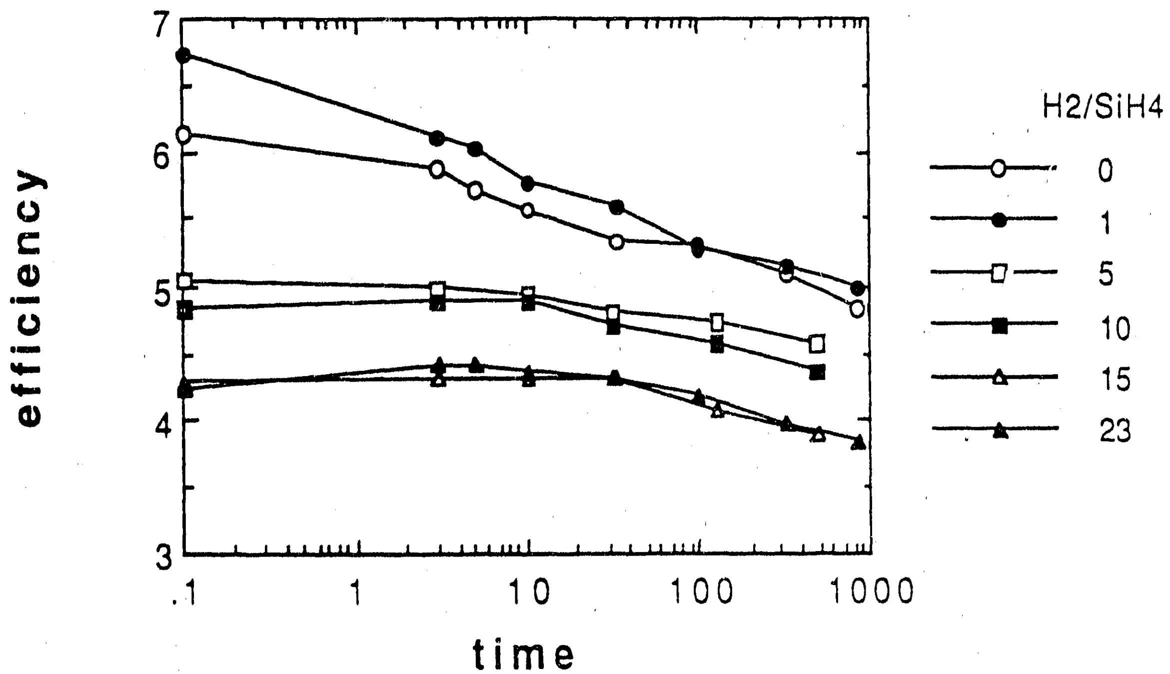

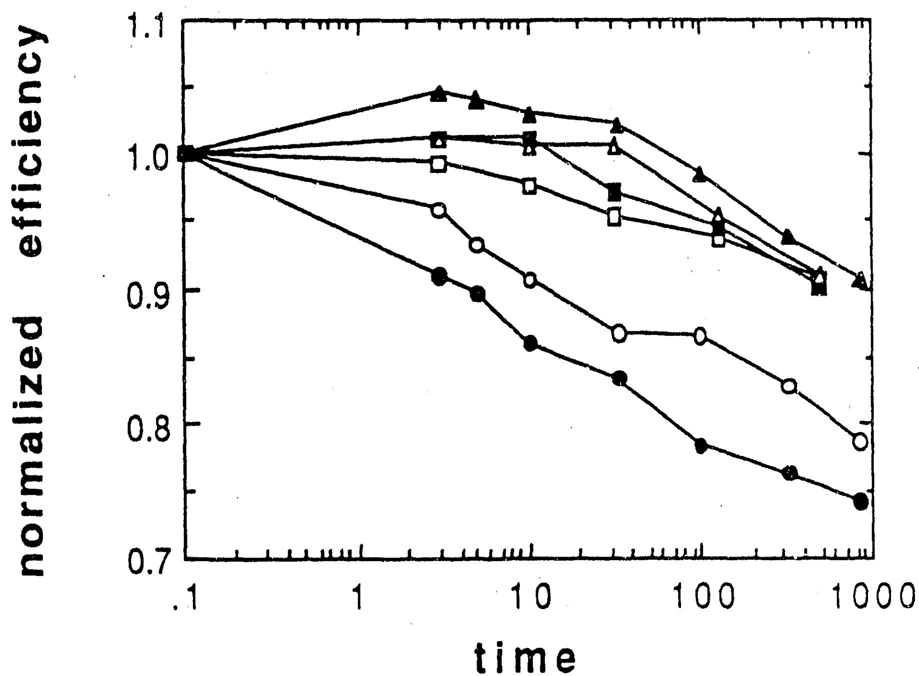

Figure 27. The absolute and normalized efficiency versus the light soaking time for devices having intrinsic layers made with various hydrogen dilutions

2.4 Thin Microcrystalline P-Layers

Using μc-p layers is generally thought to be a very efficient way to enhance V_{oc}. However, very little progress has been made on the device performance of TCO/μc-p structures. We believe the problem is related to the nucleation of the μc grains. Figure 28 shows the conductivity vs. layer thickness of μc-p layers on different substrates. The data suggest that the initial layers tend to be amorphous.

We annealed such a p-layer recently for several days at 600°C in a N_2 environment. Before annealing, the film had a conductivity of 3×10^{-3} Scm^{-1} and an activation energy of 0.11 eV. The film thickness was about 330Å, the substrate was Corning 7059 glass. We believe that the initial film was a mixture of microcrystalline and amorphous material. After annealing, the conductivity of the film increased to 55-70 Scm^{-1}, more than four orders of magnitude. The activation energy was lowered to 0.017 eV. This result shows that annealing can produce very conductive, very thin microcrystalline or polycrystalline layers.

More work was carried out on solid phase, crystallized thin microcrystalline p-layers. We deposited a-Si:H,B p+ layers from a SiH_4 and B_2H_6 gas mixture, then furnace annealed the film in a N_2 environment at 600°C. The film thickness was about 300Å to 400Å. After annealing, the conductivity of the film reached ~90 Scm^{-1}. This very high conductivity suggests that the film is completely crystallized.

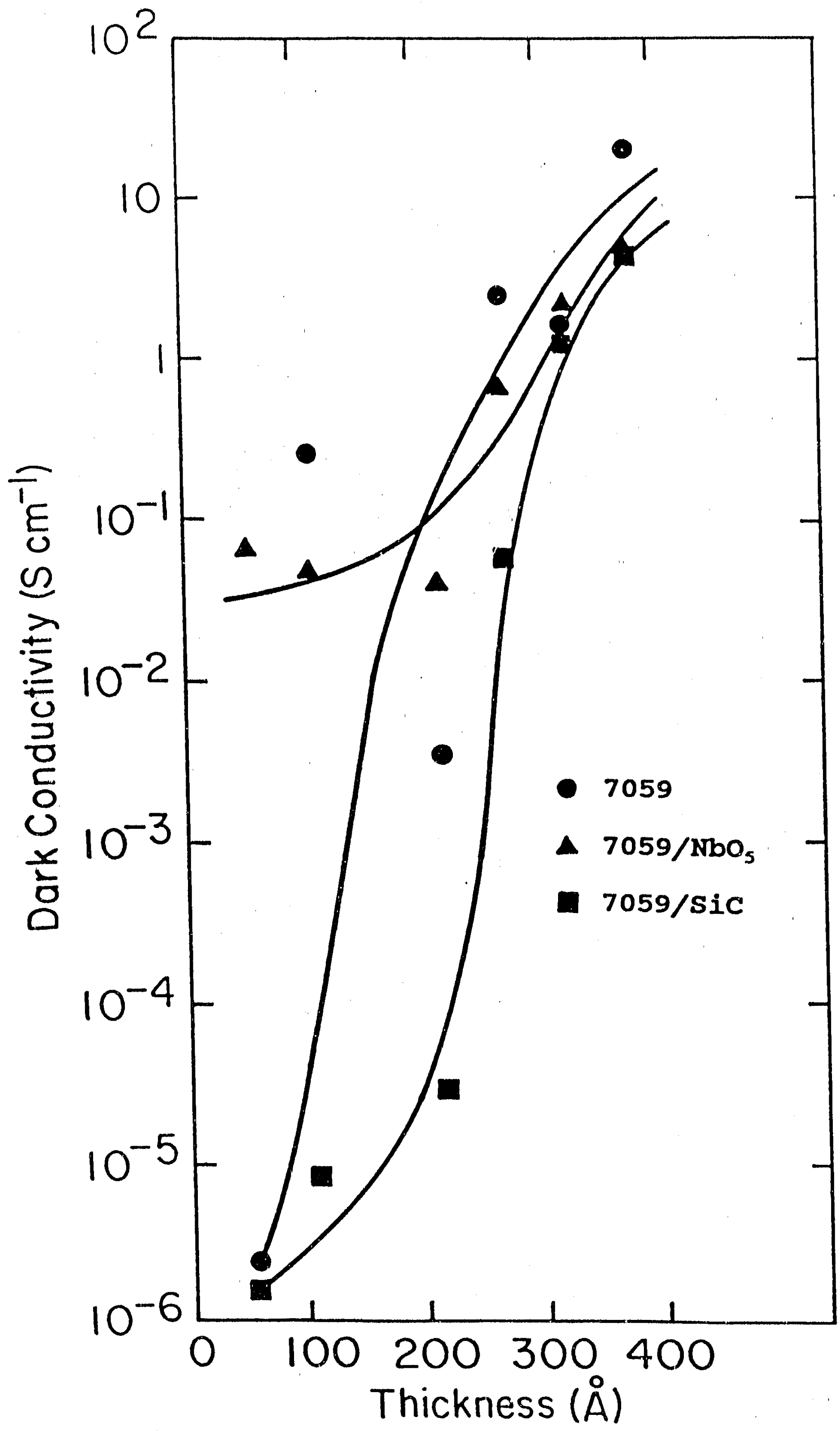

Figure 28. The conductivity of microcrystalline p-layers versus the thickness.

We also deposited a-SiC:H,B film from a gas mixture of SiH_4, $B(CH_3)_3$ and CH_4. After annealing under similar conditions, the conductivity of the film was raised from 1.6×10^{-6} to 1.3×10^{-5} Scm^{-1}. This result confirmed that carbon impedes the crystallization of the film. To provide nucleation centers, we deposited two layers: a-SiC:H,B and a-Si:H,B. Annealing under the same conditions produced a film with a conductivity of 2.2×10^{-3} Scm^{-1}. We think the material still is a mixture of amorphous and crystalline phases.

The same films (a-Si:H,B and a-SiC:H,B) have been deposited on TCO coated glass. During annealing, the films turned dark first (might be due to hydrogen evolution and band gap shrinkage), then gradually turned very transparent. We suspect that some chemical reaction happened during annealing, e.g., Si reacted with SnO_2, producing SiO_2 and Sn (Sn might evaporate from the surface).

2.5 Device Modeling

Device modeling work was carried out to analyze the losses and point out the direction for efficiency improvement. The model takes a transmission which can be determined experimentally, and calculates the absorption in different semiconductor layers by Tauc's formula. The effect of the back reflector is considered by using multiple optical paths. For the model here, we assumed p-layer thickness of 100Å (E_g = 2.1eV), and n-layer thickness of 150Å. The bottom cell thickness was fixed at 3500Å, and the top cell thickness was calculated to give a matching current. The reflectivity of Ag was assumed to be 95%.

Figure 29 shows the normalized optical absorption in various layers in a solar cell. The result is very similar to that published by other groups[3]. It is clear that the major optical loss is in the non-semiconductor part, that is, the loss at the front (reflection, glass absorption, TCO absorption) and back. For the semiconductor part, the loss in the doped layer is relatively small. However, the band gap of the i-layer for the bottom cell has a strong effect.

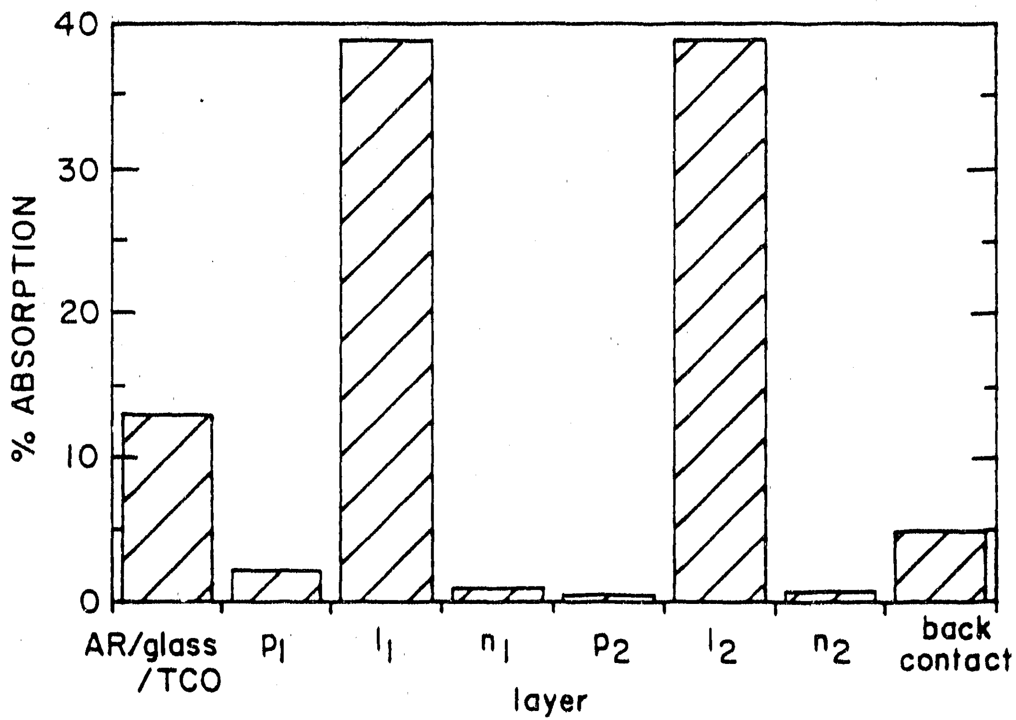

Figure 29. The modeled photon absorption in each layer of a tandem.

Figure 30 shows the modeled (matching) current vs. the bandgap of the bottom cell. It is clear that when the gap of the bottom cell decreased from 1.77 eV to 1.70 eV, the matching current increased from 7.17 mA/cm^2 to 8.05 mA/cm^2 (12%). Curve (b) corresponds to an improved back reflector (increased optical path and reflectivity). Note that the point at 1.77 eV bottom cell is our status when the program started. If we can further increase the optical transmission from 87% (which is assumed for curves a) and b) to 92%, the matching current can be further increased (curve c). Note that the highest current obtained here is about 8.8 mA/cm^2, which is close to the current reported by the Fuji group.[4]

Figure 31 shows the modeled QE and I-V curve for our current cell. Figure 32 shows the same for our future cell. Figure 33 shows the I-V curve for the future cell with improved p-layer (higher V_{oc}) and i-layer (better FF).

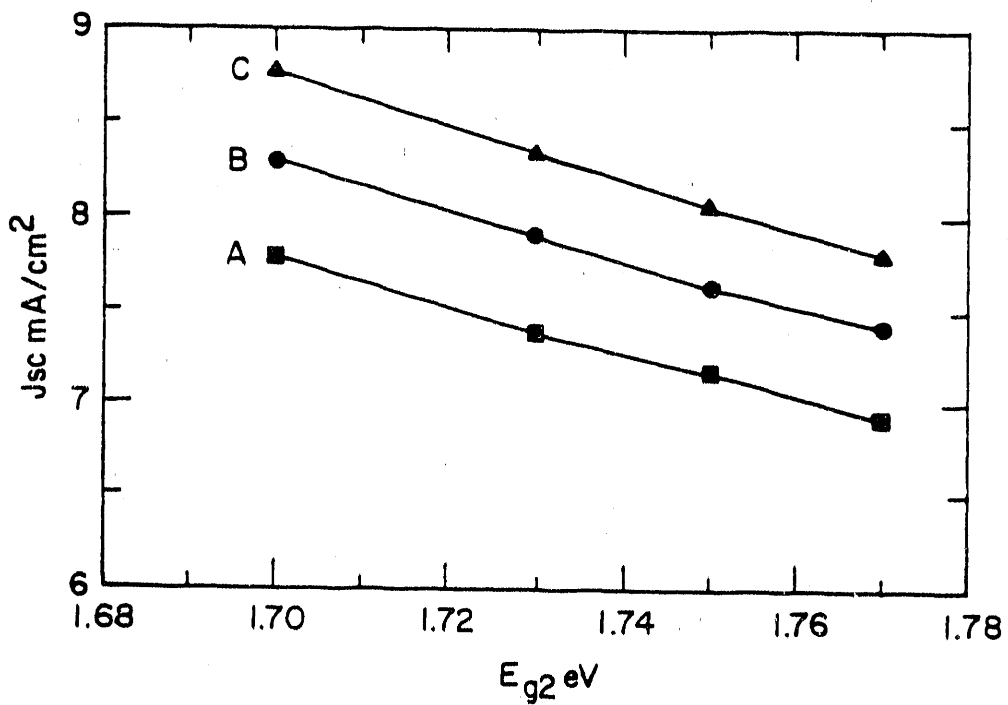

Figure 30. The modeled short circuit current versus the band gap of the bottom cell.

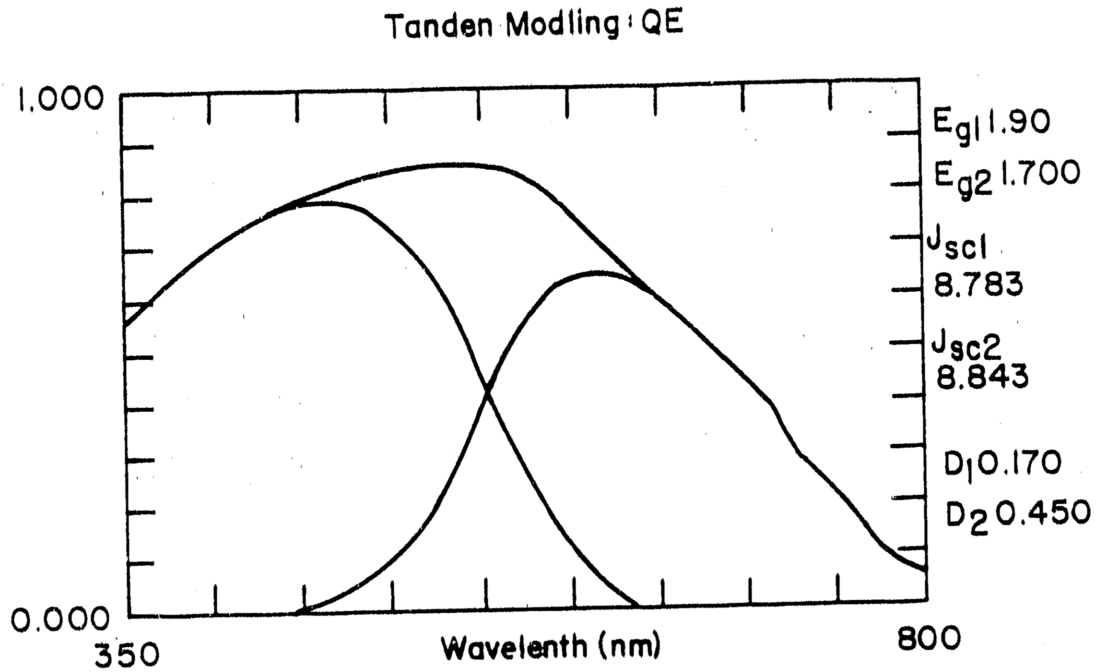

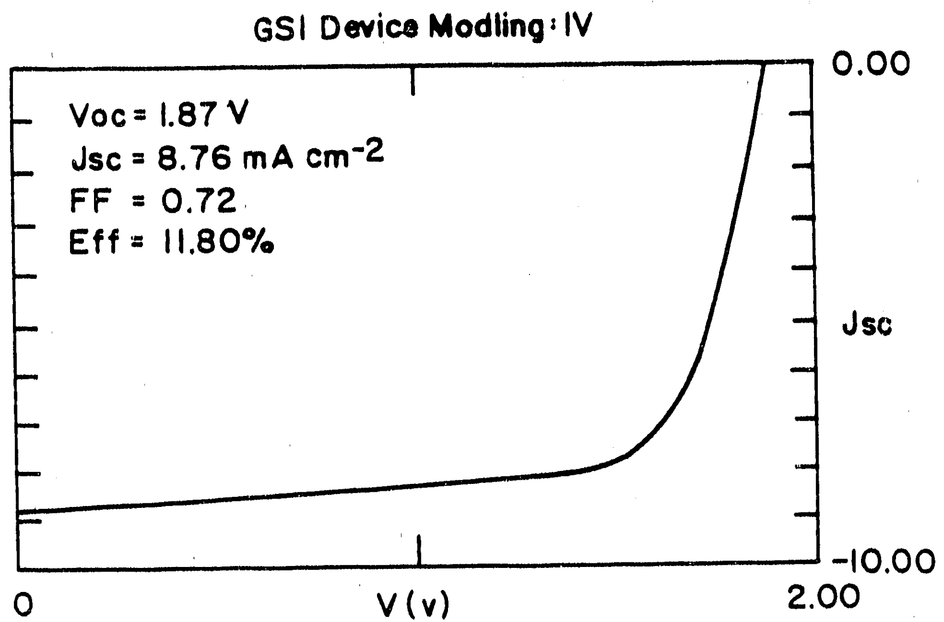

Figure 31. The modeled QE and IV of current tandem cells.

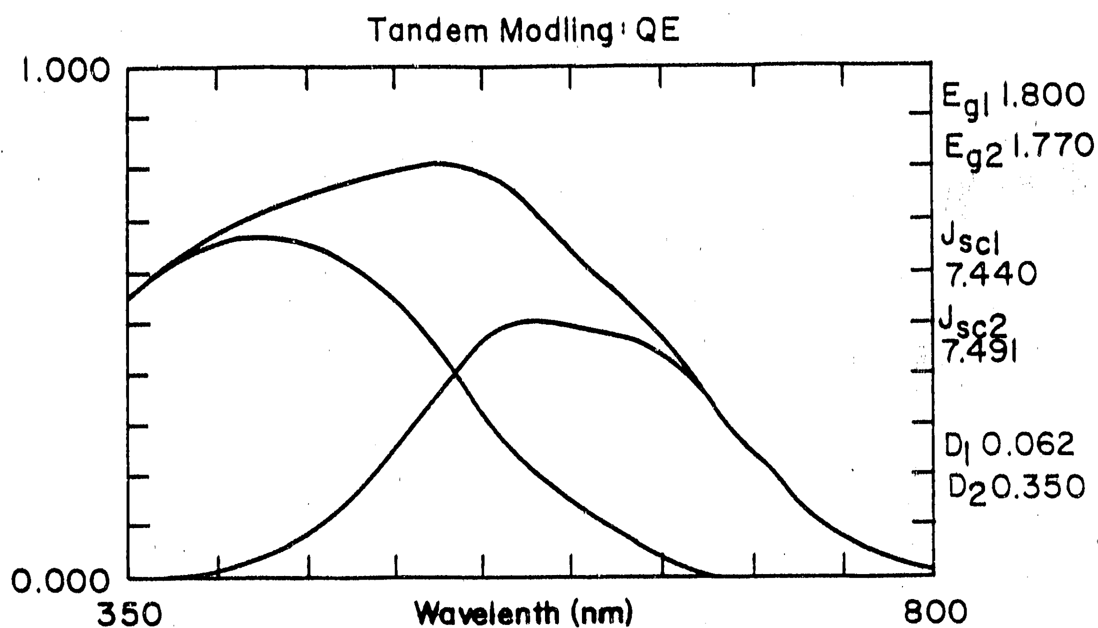

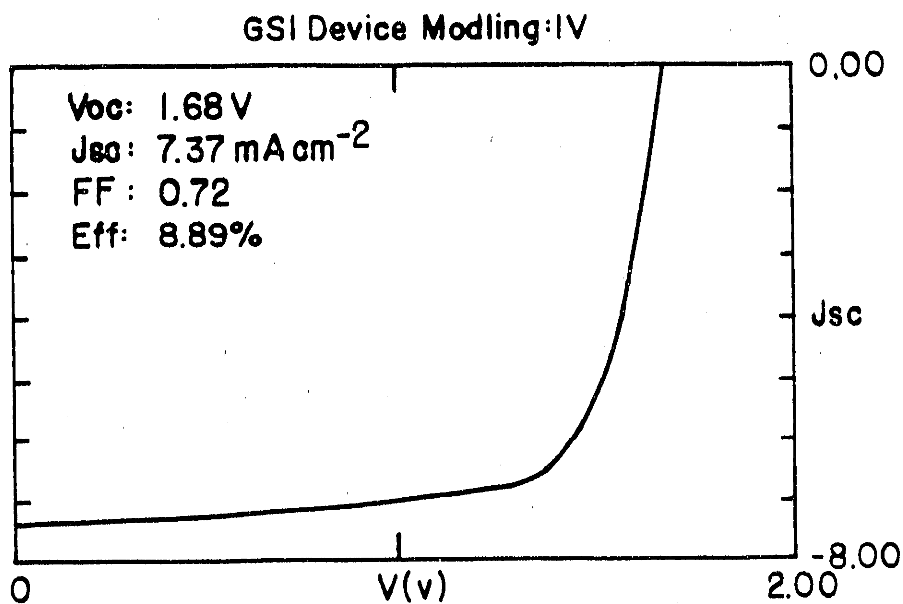

Figure 32. The modeled QE and IV of future tandem cells.

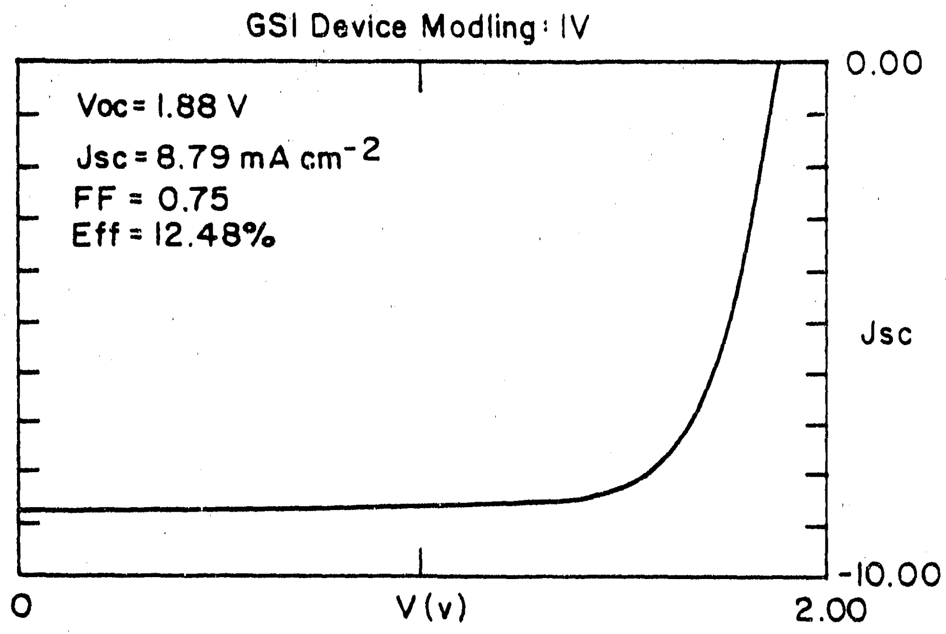

Figure 33. The modeled IV of the final goal tandem cell.

3.0 TASK II: NON-SEMICONDUCTOR RESEARCH

3.1 ITO/Ag Back Reflector

More work was done on the ITO/Ag back reflector. For all cells mentioned in Section 2, Ag and ITO/Ag back reflectors were used as back contacts. Figure 34 shows a comparison of the current density using these two back reflectors; the current density can be increased about 1-2 mA/cm2 by using ITO/AG. The mean value and standard deviation of the photovoltaic parameters are shown in Table 4 for ITO/Ag and Ag contacts. The intrinsic layer deposition conditions are slightly different for each of the 10 runs, so the standard deviation gives a measure of the sensitivity to intrinsic deposition conditions. As a comparison of ITO/Ag versus Ag, the mean value of the difference between ITO/Ag and Ag in the same run is also shown in Table 4. There is possibly a slight increase in V_{oc} with ITO/Ag and a slight drop in fill factor. The current increase is 1.76 ± 0.56 mA/cm^2 and there is an absolute gain in efficiency of 1%. There is less variation of the ITO/Ag devices as seen from the smaller standard deviations for current and efficiency. This might be due to a more consistent value of reflectivity from run to run with ITO/Ag as opposed to Ag. The reason that some samples show only a small increase is not clear yet. We speculate that it might be due to the sputtering process of ITO (change in properties of ITO) or due to the higher absorption in the cell (those with a small increase with ITO/Ag have a higher current density with Ag).

Table 4 Initial performance of devices with Ag and ITO/Ag back contacts. The column labeled "ITO/Ag-Ag" is obtained by subtracting the performance within each run.

	ITO/Ag	Ag	ITO/Ag-Ag
V_{oc} (Volts)	0.822 ± 0.012	0.814 ± 0.016	0.008 ± 0.006
J_{sc} (mA/cm^2)	15.55 ± 0.34	13.79 ± 0.55	1.76 ± 0.56
FF	0.688 ± 0.015	0.694 ± 0.014	0.006 ± 0.010
η (%)	8.79 ± 0.30	7.79 ± 0.42	1.00 ± 0.27

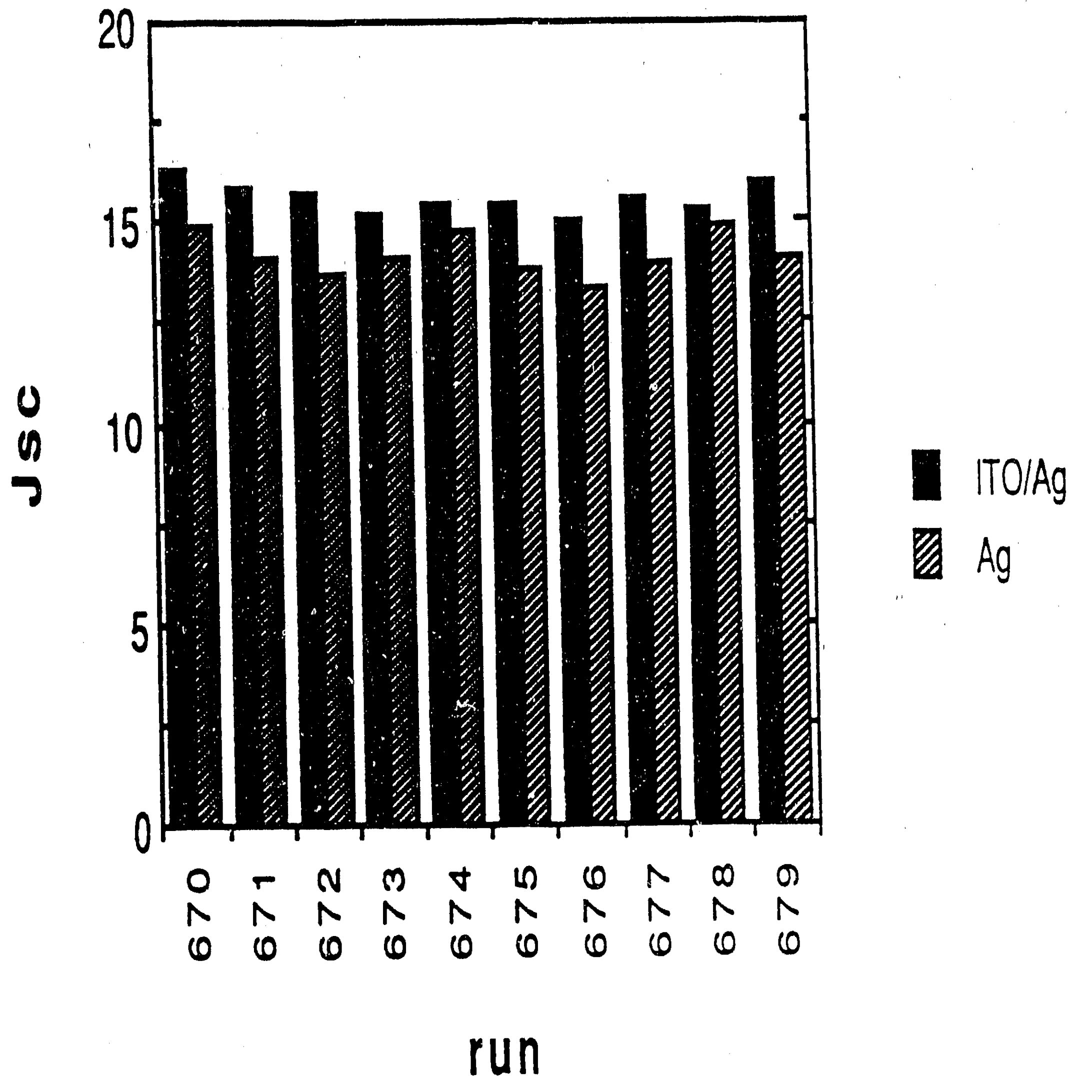

Figure 33. The short circuit current for devices with ITO/Ag and Ag top contacts

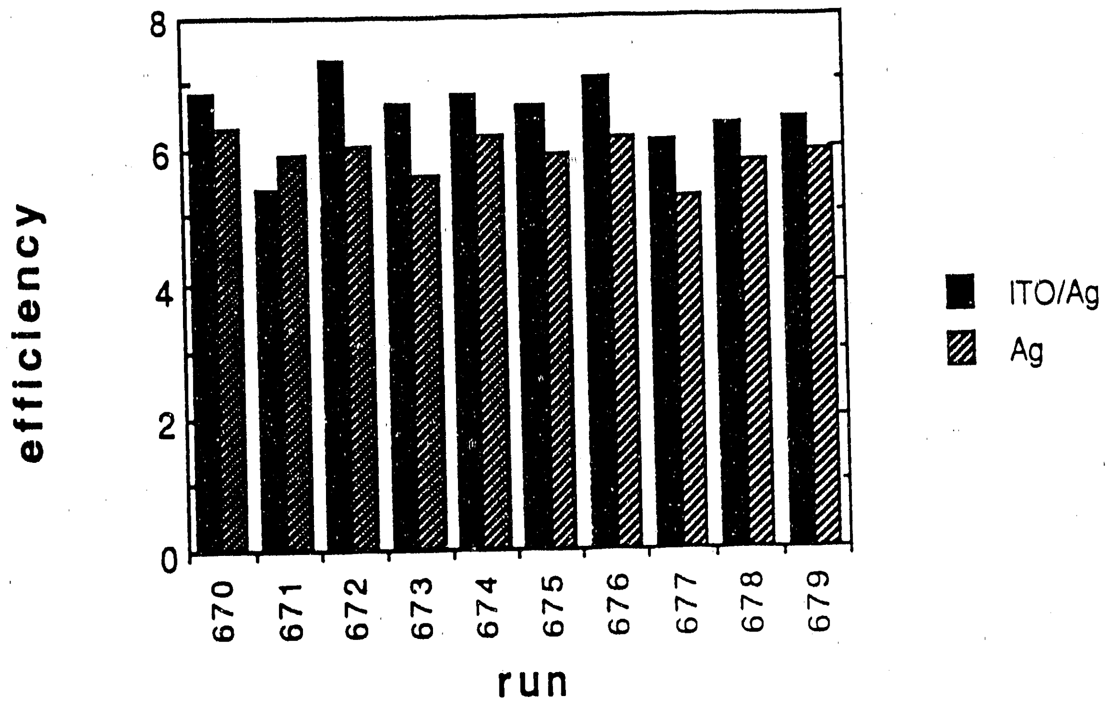

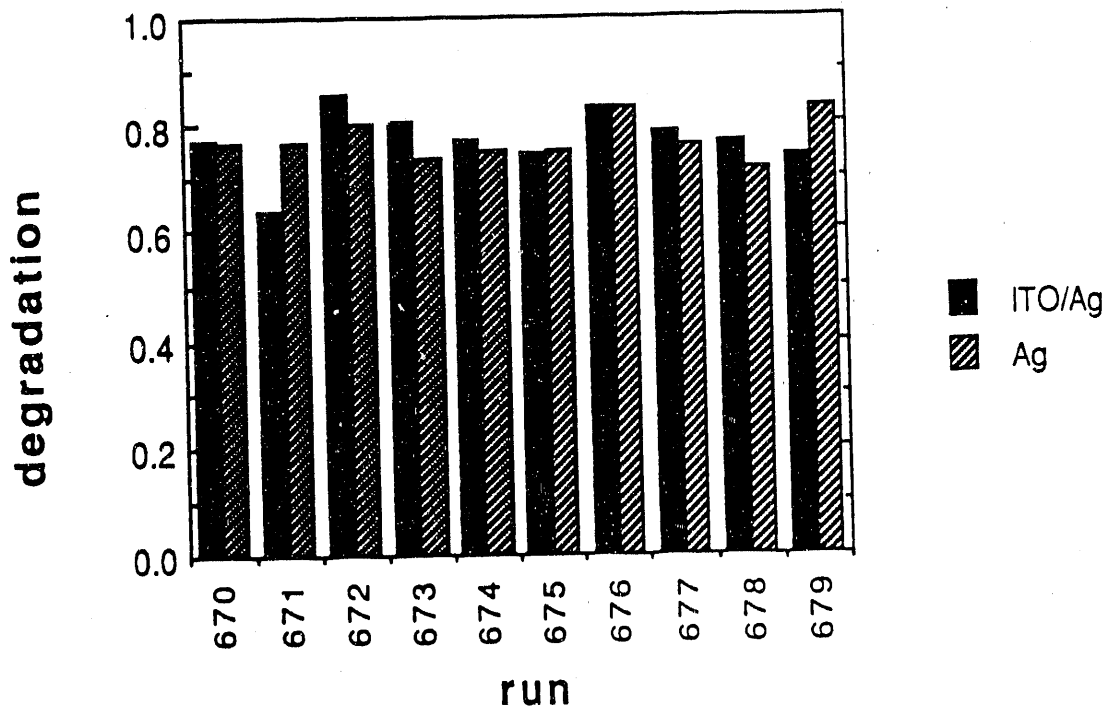

Figure 34. The efficiency and percent degradation after 300 hours for devices with ITO/Ag and Ag top contacts

3.2 Stability of Top Contacts

Figure 35 compares the absolute efficiency and percent degradation after 300 hours of light soaking of devices from 10 runs having Ag and ITO/Ag top contacts. In only one case is the degraded efficiency of the ITO/Ag device lower than the Ag device, and that was due to the ITO/Ag device partially shorting sometime during the light soaking. Overall, in this sequence devices with ITO/Ag contacts exhibited less degradation than identical devices having Ag contacts.

3.3 Transparent Conductive Oxide

3.3.1 Equipment and Process Description

The GSI-CGC TCO plant deposition equipment is very similar to its predecessor, the GSI-BHEL deposition equipment, which was manufactured for GSI by Asahi Glass Co. (AGC) of Japan. The conveyorized furnace body of the CGC equipment was manufactured by Glasstech, Inc. (Ohio), following very closely the design of the BHEL furnace, while the gas handling and delivery system was manufactured by GSI. Both these equipments are very similar in functional design characteristics to Watkins-Johnson conveyorized furnaces for TCO deposition.

The source materials for this furnace include both gases and liquids. There are two thin film layers, SiO_2, and SnO_2;F, that are deposited by atmospheric-pressure-chemical-vapor-deposition (APCVD). The furnace has two gas injectors, one for SiO_2 and one for SnO_2. The SiO_2 layer is between 800-1000Å, and serves as a sodium anti-diffusion barrier. During the course of the runs, the SiO_2 layer was made from a standard recipe and was kept constant. The parameters varied were those for the SnO_2 injector, described below. The basic reaction for tin oxide deposition is:

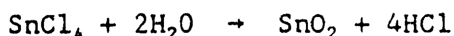

$$SnCl_4 + 2H_2O \rightarrow SnO_2 + 4HCl$$

The SnO_2 injector is a device for gas distribution which spreads the reactant gases and vapors as a line source with an orientation

perpendicular to the direction of travel of the glass, and along its width. This injector is depicted in Figure 36. It consists of a set of plates with machined holes that are then sandwiched together to form a unit which functionally acts to bring the reactants to the glass surface in a set of five laminar sheets of gas. In the center sheet flow the tintetrachloride vapors diluted in nitrogen; in the outer two sheets flow water and methanol vapors diluted in nitrogen, and in the two sheets between these sheets flow the separation nitrogen with HF mixed in.

The idea is to bring the reactants to the surface of the heated glass, in a laminar fashion perpendicular to the surface. The separation nitrogen acts to prevent the mixing of the $SnCl_4$ in the center sheet and the H_2O in the outer two sheets, until these reach the glass surface. Methanol is used to moderate the reaction and it has dramatic effects on film properties; methanol is not depleted in the reaction. HF is used to dope the SnO_2 with fluorine, and it too strongly affects the reaction and film properties.

The source materials for the SnO_2 injector are all liquids at 20°C. Pure (99.9%) HF is drawn from the tank and brought in heated stainless steel gas lines up to a mass flow controller which is also heated and then through a heated line out to the injector, where it is brought in with the separation nitrogen. The tintetrachloride ($SnCl_4$), water (H_2O) and methanol (CH_3OH) are obtained by bubbling dry nitrogen through bubblers containing these liquids. The bubblers sit in oil baths which are carefully controlled in temperature with PID digital controllers.

The actual temperature of the glass under the SnO_2 injector is 550°C ± 20°C, while just prior to the injector, it is 580°C ± 20°C. From the basic reaction given above, one would expect to have a flow of water equal to twice that of the tin tetrachloride. As it turns out, the ratio of these two with flows and temperatures given above, turns out to be closer to 44 ($H_2O/SnCl_4$). It is typical in APCVD furnaces to have large flow ratios of the reactants and to have a large deposition rate and a high utilization rate of the source material.

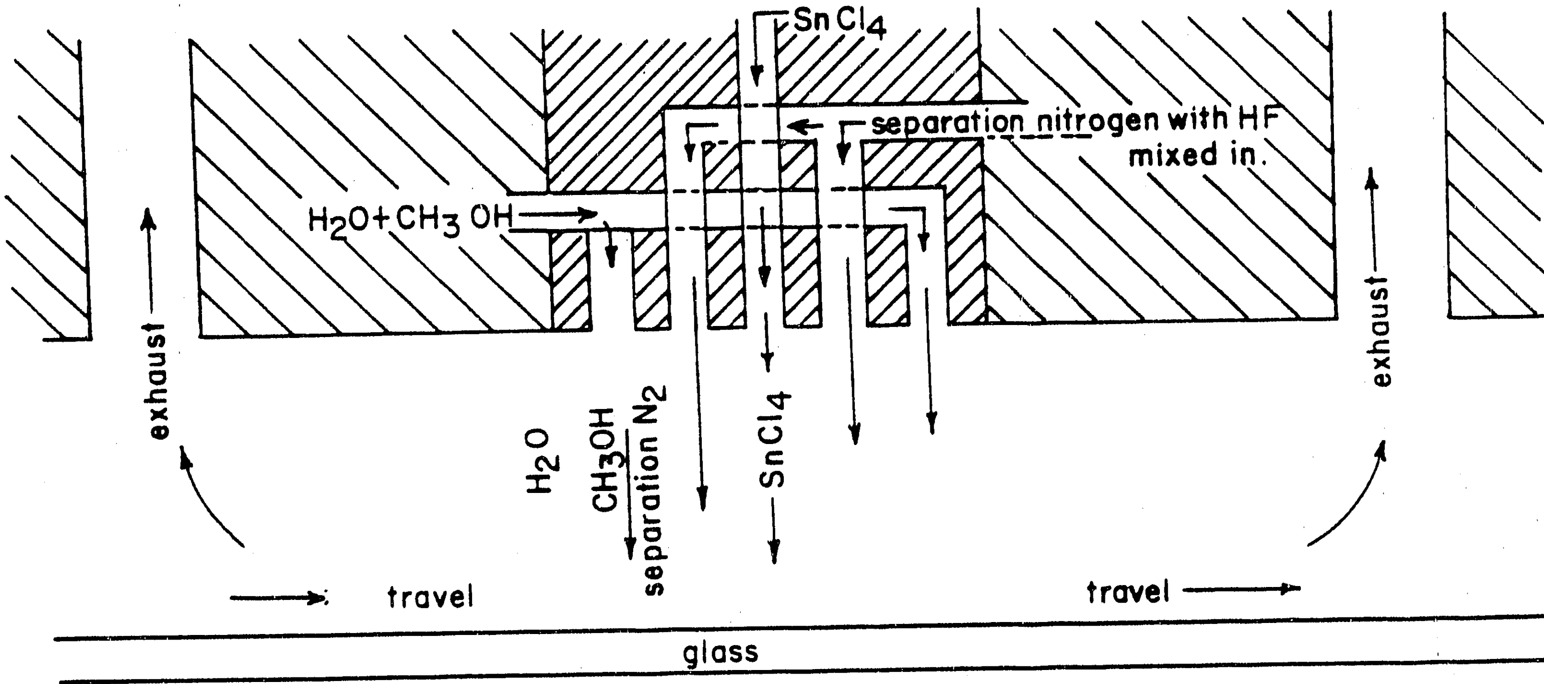

Figure 36. The tin oxide injector schematic.

The furnace was brought up to temperature and allowed to stabilize for at least three hours prior to any depositions. The gas lines were purged with N_2 for about 30 minutes prior to deposition. The bubblers were always kept on and hot overnight. Then one would let the process stabilize by waiting 4 - 6 (120 cm) glass lengths, before coating on a "good" sample. The belt was tracked at between 45 - 48 cm/min, hence stabilization time between "good" substrates was 10 - 13 minutes. The glass used was 40 cm wide by 120 cm long by 3 mm thick soda lime glass. These pieces were loaded at the entry to the furnace from a conveyorized glass cleaning station. Typically 2 good substrates were loaded with 4 - 6 dummy substrates between, with little or no gap between substrates, save one large gap intended for sighting the change to new process conditions. After the TCO coating, the substrates were selected for characterization measurements. The 40 x 120 cm^2 glass was then cut up, and 26 representative 2-inch squares were selected. For each of the 26 squares, we measured the sheet resistance, using an Alessi 4 point probe; the total visible integrated transmission and haze, using a Suga Test Instrument (Tokyo) digital haze meter, model HGM-2DP; and the thickness using a Tencor alpha-step-200 profilometer. The data were then fed into a computer (PC/AT) for analysis. By keeping a record of where each of the 26 squares came from on the substrate, we could track non-uniformities across the substrates. The same basic procedure was used in running the furnace, doing depositions and measurements on selected substrates, when changing process parameters. We did a series of runs where we systematically varied the flows of the methanol and HF, as these showed dramatic effects on film properties.

3.3.2 Results

In Figure 37, we have plotted sheet resistance, transmission, haze, and resistivity vs. injector height above the surface of the glass. The injector height was varied between 4 and 11 mm; the absolute accuracy in this distance is indeterminate to ± 1 mm, although the relative error between measurements is ± 0.25 mm or less. As seen on Figure 37, there is a steady drop in sheet resistance, about 1.5 Ω/□ total drop in changing this height from 11 to 4 mm. The integrated transmissions and haze show no trend vs. height, at least in this regime; the resistivity shows a

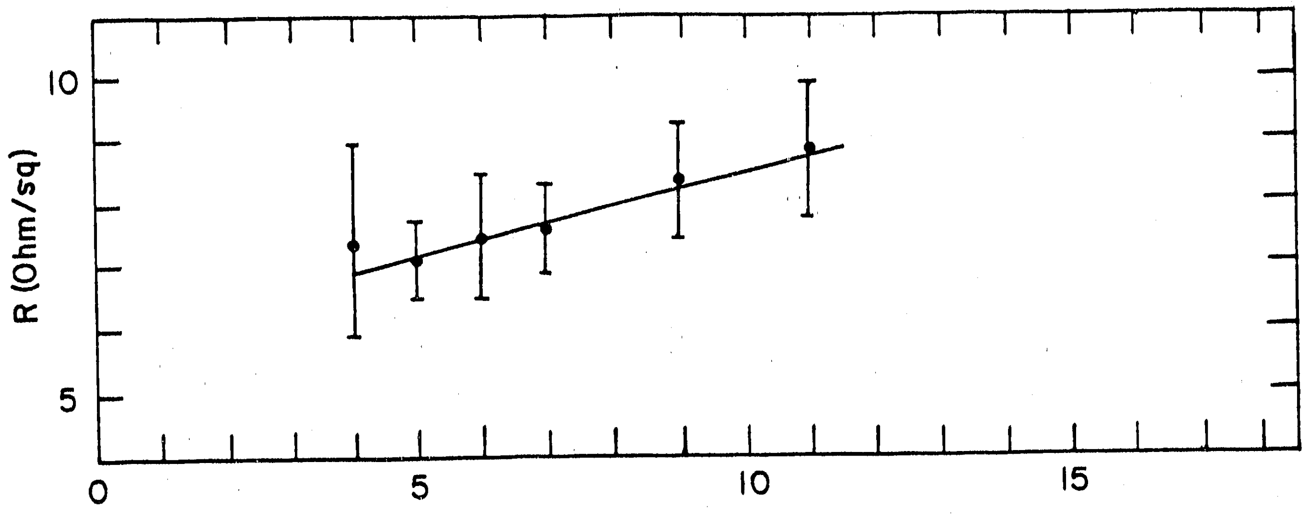

Figure 37. The tin oxide sheet resistance, transmission, haze and resistivity versus the injector height.

discernable but small drop of from $4.3*10^{-4}$ to $3.9*10^{-4}$ Ωcm; the thickness shows an increase of about 500-600Å as the SnO_2 injector is lowered. At the lowest height the scatter in the data became larger than for greater heights, as expected, since at very small distances, small warpage of the glass affects the actual distance between the glass and the injector, and hence the flows and the film growth. That the resistivity should vary with height could be interpreted as another sign that growth and growth rate are very important determining factors in the material resistivity; the variation of 40 micro-Ohm-cm with height is smaller to the same order change in resistivity as seen in some of the other experiments carried out with HF variation.

In Figure 38, we have plotted the sheet resistance, resistivity, thickness and haze, respectively, vs. methanol to water (N_2) flow ratios. It should be pointed out that a flow of zero, although not plotted, produces films which are more resistive; with both very low methanol and HF flows producing films with resistivities on the order of 10^{-3}Ωcm, or about 5 times higher resistivity, and high haze (50%), but poor transmission (<70%). As can be discerned from Figure 38, there is a trend to higher sheet resistances at both very high and low methanol flows, that is, there is some optimum methanol to water ratio, which varies with amounts of HF which is present, when optimizing resistivity and sheet resistance. The thickness appears to vary little (< 500 Å) with methanol flow. The haze varies considerably with methanol, and the dashed lines in Figure 38 are drawn to group families of curves with equal HF content. As can be seen, an increase in HF flow depresses the formation of haze. Increasing the methanol flow, however, increases the haze for a given flow of HF, at least in this regime. We also know that at very low HF and methanol flows, the haze produced at these glass temperatures (550-580°C) is large, and hence some of the dashed curves on Figure 38, turn up and move asymptotically to about 50% for zero methanol flow.

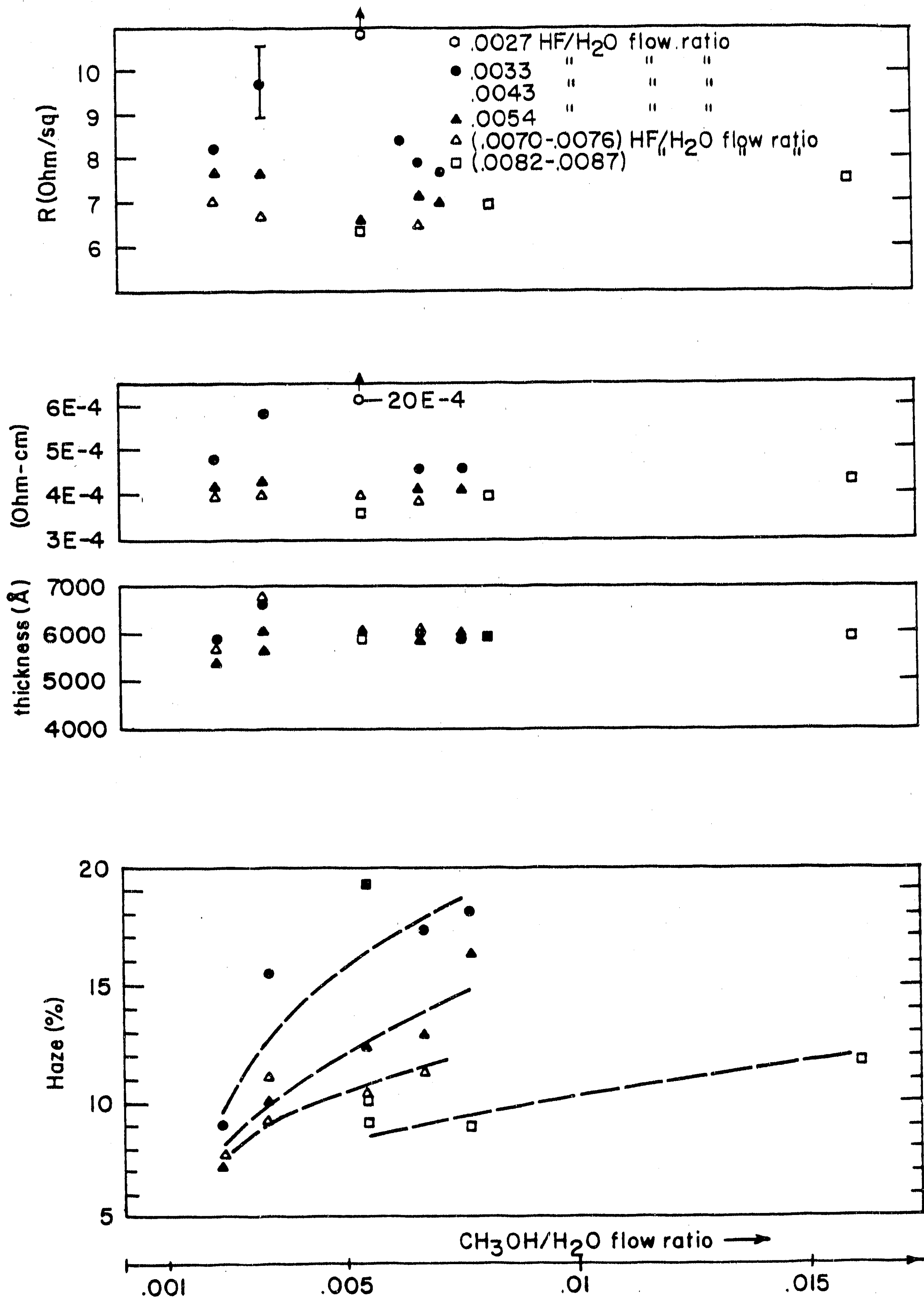

Figure 38. The tin oxide sheet resistance, resistivity, thickness and haze versus the methanol to water ratio.

4.0 TASK III: MODULE RESEARCH

We used our CGC line to fabricate a-Si/a-Si dual-junction modules. The purpose was to identify the technical problems in making very large area (4800 cm^2) dual-junction modules.

The modules show reasonably good performance, with subcell active area initial efficiency around 7% and subcell yield of > 80%. Two modules have been measured at SERI, the measured parameters are listed in Table 5. For comparison, the parameters of a single-junction cell are also listed.

Table 5 Parameters of large area panels measured at SERI

Type	Total area (cm^2)	FF	Voc(V)	Jsc(mA)	Peak Power(watts)
Single junction	4800	0.657	23.72	1937	30.19
Tandem, Si-Si	4800	0.604	41.23	948	23.62
Tandem, Si-Si	4800	0.600	41,77	956	23.95

Compared with the single-junction module of same size, the major loss of the dual-junction module is in the tunnling junction. Since the CGC production line does not have a section which can coat metal oxides, the I-V curves of the subcells show curvature near V_{oc} condition (Fig 39). This phenomenon has been observed before in our small area dual-junction cells, and has been corrected by inserting a thin NbO_X layer in the tunneling junction.

By using metal oxides in the tunneling junction and ITO/Ag for the back reflector, we are confident that the dual-junction module can easily reach similar performance as the single-junction modules. Further improvement can be achieved by using advanced module design.

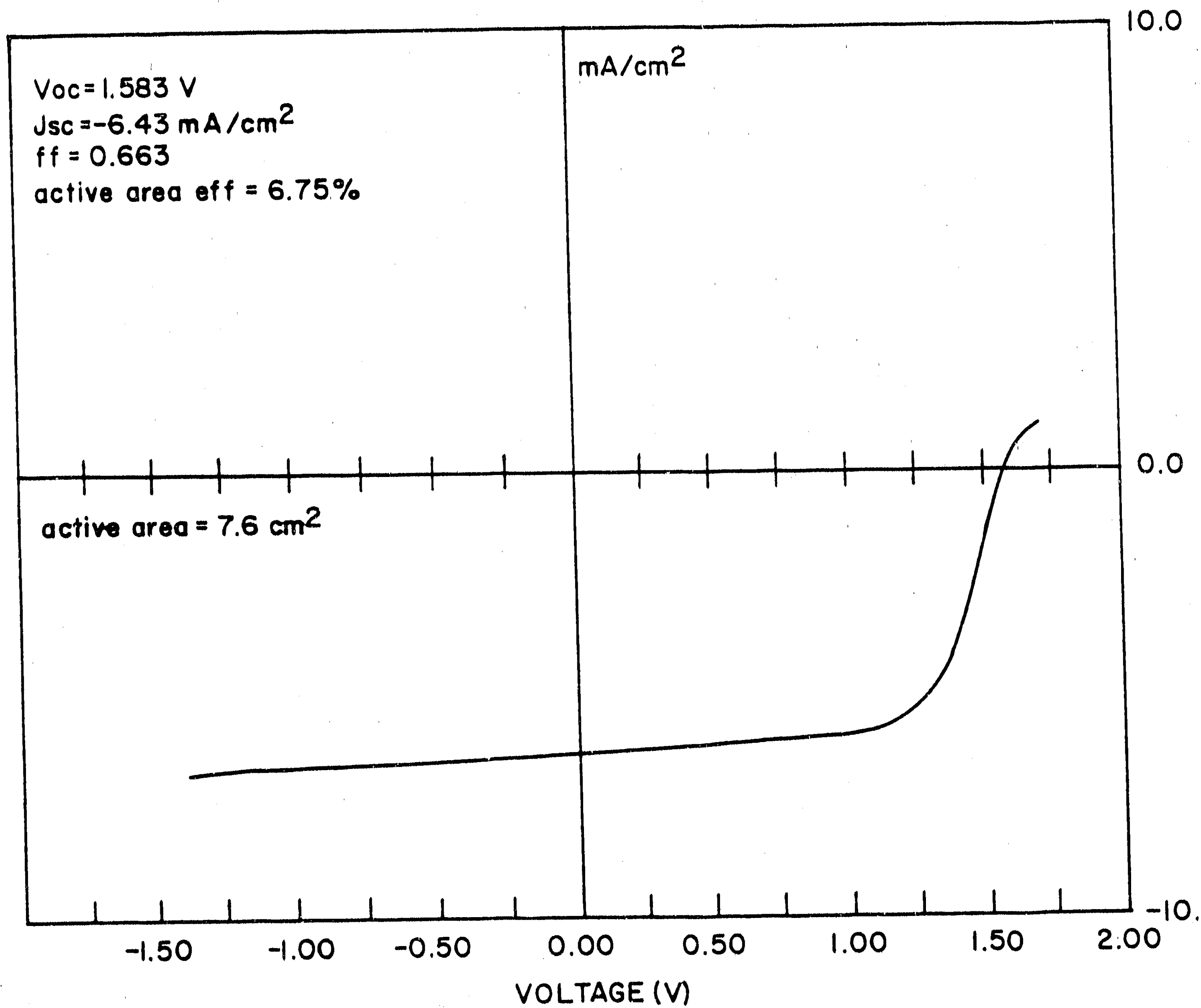

Figure 39. IV curve of a subcell of a large area ($4800cm^2$ tandem panel.

5.0 CONCLUSIONS

1) By changing the hydrogen content in the intrinsic amorphous silicon, the Tauc's gap could be changed to 1.73 eV and 1.9 eV with reasonably good material.

2) At high temperatures (>250°C) of deposition, the performance of a solar cell appears to be limited by the boron and phosphorous diffusion into the i-layer.

3) It is not clear, but we consistently found that the best initial performance of a solar cell also yields the best stabilized efficiency.

4) It is not clear whether hydrogen content has an effect on the degradation of good intrinsic material for a range of hydrogen content in the regime 9 - 16%.

5) SnO_2 produced by APCVD seems to be a robust process that can produce films with desirable conductivity and optical properties (including texture) for use in a-Si:H solar cells. However, more work on morphology of SnO_2 films is needed to enhance solar cell efficiencies.

6) The ITO/Ag contact seems to be a stable contact for a-Si:H solar cells.

7) Progress toward the goal has been good, with the demonstration of a 5.4% initial efficiency in a silicon-silicon multijunction module having an aperture area of 4620 cm^2 and incorporating devices with second junction i-layer thicknesses of 3500Å. Moreover, a single-junction silicon module having an aperture area of 4620 cm^2 and a thickness of 3500Å with an initial efficiency of 6.5% was demonstrated. Although there were no stability experiments performed on these modules, a comparison with small-area stability results indicates the efficiency of silicon-silicon multijunction modules should approach 4.4% after 600 hours of light soaking.

REFERENCES

1. C. C. Tsai, G. B. Anderson, and R. Thompson, Materials Research Society Proceedings, Vol. 192 (1990), p. 475.

2. GSI unpublished data.

3. A. Catalano, Proceedings of the 21st IEEE Photovoltaic Specialists Conference, Kissimee, Florida (1990), p. 36.

4. Y. Ichikawa, S. Fujikake, T. Yoshida, T. Hama, and H. Sakai, Proceedings of the 21st IEEE Photovoltaic Specialists Conference, Kissimee, Florida (1990), p.1475.

Document Control Page	1. SERI Report No. SERI/TP-214-4292	2. NTIS Accession No. DE91002159	3. Recipient's Accession No.

4. Title and Subtitle Research on Stable, High-Efficiency Amorphous Silicon Multijunction Modules	5. Publication Date April 1991
	6.
7. Author(s) P.K. Bhat, S. Brown, R. Hollingsworth, D.S. Shen, J. del Cueto, E. Iwanicko, C. Marshall, C. DeHart, D. Mentor, A. Benson, C. Matovich, J. Sandwisch	8. Performing Organization Rept. No.
9. Performing Organization Name and Address Glasstech Solar, Inc. Golden, Colorado	10. Project/Task/Work Unit No. PV141101
	11. Contract (C) or Grant (G) No. (C) ZM-0-19033-3 (G)
12. Sponsoring Organization Name and Address Solar Energy Research Institute 1617 Cole Blvd. Golden, CO 80401	13. Type of Report & Period Covered Technical report
	14.

15. Supplementary Notes
SERI technical monitor: W. Luft, (303) 231-1823

16. Abstract (Limit: 200 words)

This report describes a contract to produce multijunction modules based entirely on amorphous silicon alloys, the modules having an aperture area of at least 900 cm^2 and a stable, reproducible conversion efficiency of at least 6.5% after 600 hours of light exposure (air mass 1.5) at 50° C. The work focussed on (1) producing opto-electronic-grade amorphous silicon material for band gaps of about 1.7 and 1.9 eV by changing the hydrogen content in the film bonded to the silicon, (2) studying and obtaining data on the light stability of single-junction p-i-n solar cells with gaps of about 1.7 and 1.9 eV, and (3) analyzing losses in a silicon/silicon multijunction cell. We report new results on an indium tin oxide (ITO)/silver back contact and the deposition of granular tin oxide by atmospheric-pressure chemical vapor deposition. Progress toward module fabrication at the end of six months has been good, with the demonstration of 5.4% initial efficiency in a silicon/silicon multijunction submodule with an aperture area of 4620 cm^2 and incorporating devices with 2nd-junction i-layer thicknesses of about 3500 Å. We also demonstrated a single-junction silicon submodule with an aperture area of 4620 cm^2, a thickness of about 3500 Å, and an initial efficiency of 6.5%.

17. Document Analysis
a. Descriptors
photovoltaics ; solar cells ; amorphous state ; silicon

b. Identifiers/Open-Ended Terms

c. UC Categories
271

18. Availability Statement National Technical Information Service U.S. Department of Commerce 5285 Port Royal Road Springfield, VA 22161	19. No. of Pages 69
	20. Price A04

Form No. 0069E (6-30-87)